Truncated radial glia as a common precursor in the late corticogenesis of gyrencephalic mammals

Running title: Binary fates of tRG in corticogenesis

Authors list

Merve Bilgic[1,2,3], Quan Wu[1,4*],Taeko Suetsugu[1,4], Atsunori Shitamukai[1,5], Yuji Tsunekawa[1,6], Tomomi Shimogori[7], Mitsutaka Kadota[8], Osamu Nishimura[8], Shigehiro Kuraku[8,9], Hiroshi Kiyonari[10], and Fumio Matsuzaki[1,2,4*]

Affiliations

[1]Laboratory for Cell Asymmetry, RIKEN Center for Biosystems Dynamics Research, Kobe, Hyogo 650-0047, Japan.

[2]Laboratory of Molecular Cell Biology and Development, Department of Animal Development and Physiology, Graduate School for Biostudies, Kyoto University, Kyoto 606-8501, Japan.

[7]Molecular Mechanisms of Brain Development, RIKEN Center for Brain Science, Wako, 17 Saitama 351-0198, Japan.

[8]Laboratory for Phyloinformatics, RIKEN Center for Biosystems Dynamics Research, Kobe, Hyogo 650-0047, Japan.

[10]Laboratory for Animal Resources and Genetic Engineering, RIKEN Center for Biosystems Dynamics Research, Kobe, Hyogo 650-0047, Japan.

[*]Corresponding authors

go.quan.8w@kyoto-u.ac.jp

matsuzaki.fumio.2w@Kyoto-u.ac.jp

Further information and requests for resources and reagents should be directed to and will be fulfilled by the lead contact, Fumio Matsuzaki (matsuzaki.fumio.2w@Kyoto-u.ac.jp)

[3]Present address: The Institute for Quantitative Biosciences, The University of Tokyo, Tokyo 113-0033, Japan.
[4]Present address: Department of Aging Science and Medicine, Medical Innovation Center, Graduate School of Medicine, Kyoto University, Kyoto 606-8507, Japan.
[5] Present address: Department of Human Morphology, Graduate School of Medicine, Dentistry and Pharmaceutical Sciences, Okayama University, Okayama 700-8558, Japan.
[6]Present address: Division of Molecular and Medical Genetics, Center for Gene and Cell Therapy, The Institute for Medical Science, The University of Tokyo, Tokyo 108-0071, Japan.
[9]Present address: Molecular Life History Laboratory, Department of Genomics and Evolutionary Biology, National Institute of Genetics, Mishima, Shizuoka 411-8540, Japan.

Character count (excluding materials and methods, references, and figure legends): 34742

ABSTRACT

The diversity of neural stem cells is a hallmark of the cerebral cortex development in gyrencephalic mammals, such as Primates and Carnivora. Among them, ferrets are a good model for mechanistic studies. However, information on their neural progenitor cells (NPC), termed radial glia (RG), is limited. Here, we surveyed the temporal series of single-cell transcriptomes of progenitors regarding ferret corticogenesis and, found a conserved diversity and temporal trajectory between human and ferret NPC, despite the large timescale difference. We found truncated RG (tRG) in ferret cortical development, a progenitor subtype previously described in humans. The combination of *in silico* and *in vivo* analyses identified that tRG differentiate into both ependymal and astrogenic cells. Via transcriptomic comparison, we predict that this is also the case in humans. Our findings suggest that tRG plays a role in the formation of adult ventricles, thereby providing the architectural bases for brain expansion.

Keywords:

Single-cell transcriptome / neural stem cell / brain development / ferret / human / neurogenesis / truncated radial glia.

INTRODUCTION

A vast diversity of neurons and glia form functional neural circuits during the development of the cerebral cortex in mammals. These cells are progressively generated from multipotent neural stem cells, termed radial glia (RG), following genetic processes common across species, from initially neurons of the deep layers (DL), then neurons of the upper layers (UL), and finally glial cells, astrocytes, or oligodendrocytes (**Fig. S1A, S1B**; Rowitch and Kriegstein, 2010). These processes are also spatially organized with RG divisions in the ventricular zone (VZ), IPC-neuron differentiation in the sub-VZ (SVZ), and neuron migration to the cortical plate in an inside-out manner. In many mammalian phylogenic states, cerebral cortex evolved to gain an additional germinal layer (outer SVZ (OSVZ); Smart et al, 2002), where extensive neurogenesis and gliogenesis of oRG occur (Hansen *et al*, 2010; Fietz *et al*, 2010; Reillo *et al*, 2011; Gertz & Kriegstein, 2015) resulting in the amplification of neuronal and glial populations in the cortex (**Fig. S1**; Rash et al, 2019). On the other hand, a new subtype of NPC in the VZ has recently been reported in humans and rhesus macaques (deAzevedo et al, 2003;

Nowakowski et al, 2016; Sidman and Rakic, 1973), lacking the basal attachment and is therefore termed truncated RG (tRG). However, how widely tRG appears in gyrencephalic (or even lissencephalic) mammal development, what mechanisms underlie their formation, and what they produce remain unknown. As distinct NPC subtypes may possess different capacities to generate differentiated progenies (Huang et al, 2020; Rash et al, 2019), it would be critical to find answers to those questions to understand commonality and diversity in the mammalian brain evolution.

Genetic manipulation of individual cell types *in vivo* and single-cell transcriptome analysis are two major and successful approaches in revealing the properties of cells, such as their proliferation and differentiation. Thus, single-cell RNA sequencing (scRNA-seq) of the human brain during development has been extensively performed (Herring *et al*, 2022; Bhaduri et al, 2020, 2021; Huang et al, 2020; Johnson et al, 2015; Liu et al, 2017; Polioudakis et al, 2019; Pollen et al, 2015; Zhong et al, 2018). However, the *in vivo* behavior in humans and other primates and the underlying mechanisms remain less explored owing to the limited experimental access to the developing primate cortices. Particularly, resources available for the late human embryonic brain are extremely rare due to ethical challenges. Also, studies using brain organoids face issues in recapitulating the specification and maturation of cell types during human brain development (Bhaduri et al, 2020). In this context, the ferret (*Mustela putorius furo*) is highlighted as a suitable animal model, which compensates for the difficulties in studying human cortical development. Ferrets are carnivores that develop common gyrencephalic features, such as the OSVZ and a folded brain, and are frequently used in mammalian models of brain development and circuit formation because neurogenesis continues in their early neonatal stages (Chapman & Stryker, 1992; McConnell, 1988; Noctor *et al*, 1997; Jackson *et al*, 1989). Since this species is experimentally manipulable, recent studies have developed *in vivo* gene manipulation and editing technology using *in utero* electroporation (IUE; Matsui et al, 2013; Kawasaki et al, 2012; Tsunekawa et al, 2016; timelapse imaging; McConnell, 1995; Chenn & McConnell, 1995). Furthermore, ferrets showed severe microcephalic phenotypes via *ASPM* (*Abnormal Spindle-like Microcephaly-associated* gene) knockout (Johnson et al, 2018; Kou et al, 2015), which greatly differs from a minor phenotype in mouse *ASPM* knockout mutants (Capecchi and Pozner, 2015; Fujimori et al, 2014; Jayaraman et al, 2016; Pulvers et al, 2010). This remarkable finding suggests the presence of mechanisms underlying brain enlargement and circuit complexity shared by gyrencephalic species to some extent. Results from transcriptome profiling of ferret cortical

96 cells has revealed regional differences in germinal layers and cell-type composition (Johnson
97 et al, 2018; de Juan Romero et al, 2015). However, because of the incomplete genomic
98 information, especially due to the lack of genetic models, the databases with ferret data have
99 been less reliable than those with human or mice data. This has posed a limit for the accurate
100 comparison of single cell transcriptomes between ferrets and humans. Hence, the temporal
101 pattern of molecular signatures of ferret NPC remains largely unexplored at single-cell
102 resolution. Comparison of progenitor subtypes and sequential events at the single-cell
103 transcriptome level regarding development between ferrets and humans will greatly help to
104 recognize common and species-specific mechanisms underlying the construction of a complex
105 brain.
106
107 In this study, we comprehensively analyzed the developmental dynamics of progenitor
108 populations during ferret corticogenesis to clarify shared or species-specific mechanisms of
109 corticogenesis in gyrencephalic mammals and found that ferrets generate tRG at late
110 neurogenic and early gliogenic stages like humans and other primates. Analysis of the
111 pseudotime trajectory and temporal histochemical pattern suggested that tRG generate
112 ependymal and astrogenic cell fates. Then, we compared temporal series of ferret and human
113 single cell transcriptomes (Bhaduri et al, 2021; Nowakowski et al, 2017). Remarkably, we
114 found homologous temporal progenitor trajectories irrespective of the large differential
115 corticogenesis timescale. This study combining rich ferret and human transcriptome data with
116 *in vivo* analysis using ferrets emphasizes the value of single-cell ferret transcriptome datasets.
117
118 **RESULTS**
119 **Temporal patterns of neurogenesis and gliogenesis in the cerebral cortex of ferrets**
120 First, we confirmed histochemically the spatial and temporal pattern of RG, oRG, and IPC and
121 the appearance of diverse cortical neurons to determine the period in which samples were to
122 be taken for scRNA-seq (**Fig. S1**). While neurogenesis mostly terminated by P5 in the dorsal
123 cortex (**Fig. S1A, S1B**), oligodendrocyte progenitors of dorsal origin ($OLIGO2^{+}$) and RG with
124 gliogenic potential ($GFAP^{+}$) became detectable approximately at E40 and increased in number
125 postnatally (**Fig. S1C, S1D**). Based on these observations, we decided to examine single cell
126 transcriptomes at embryonic days E25, E34, and E40 and postnatal days P5 and P10, which
127 recapitulate neurogenesis and gliogenesis.
128

129 **Single-cell RNA-seq revealed subtypes of cortical cells in ferrets**

130 To identify the temporal trajectories of cell types in the course of ferret brain development
131 (schematically represented in **Fig. 1A**), we performed single-cell RNA-sequencing of ferret
132 dorsal cortex at the six developmental time points described above (**Fig. 1**). Despite several
133 previous transcriptome studies on the ferret cortex (Johnson et al, 2018; de Juan Romero et al,
134 2015), information on the ferret genome is incomplete (specifically, poor information
135 regarding the 3′-untranslated region of genes), which has impeded high resolution single-cell
136 transcriptome analyses that can offer an accurate comparison with human datasets. Thus, we
137 first improved the annotations of ferret genomic DNA sequences using Chromium droplet
138 sequencing, which tagged all contigs from a long genomic DNA in a droplet, and constructed
139 new gene models based on the improved genomic annotations (**Table S1, see also Materials**
140 **and Methods**). We performed scRNA-seq using cell populations isolated in two ways to enrich
141 the progenitor subtypes (**Fig. 1A**): (1) FACS-based sorting of the neural stem cell fraction
142 labeled with an AzamiGreen (AG)-driven *HES5* promoter (Ohtsuka et al, 2006) and (2)
143 collecting cells forming the VZ, SVZ, and intermediate zones (IZ) of cerebral cortices after
144 discarding the cortical plate (CP, **Fig. 1B, S2A**). We combined these two cell populations on
145 all the sampling stages for unbiased clustering. **Figure 1C** shows cell clustering projected in
146 the Uniform Manifold Approximation and Projection (UMAP) space (preprint: McInnes et al,
147 2018; Stuart et al, 2019). We characterized 26 transcriptionally distinct clusters from 30,234
148 ferret cortical cells through corticogenesis and detected up to 2,600 median genes per cell (**Fig.**
149 **S2B, S2C; Table S1**). After combined clustering of the two collectives of cell populations
150 prepared by independent methods, we re-separated cells into each collective at each stage, and
151 confirmed a reproducibility of clustering between two different collectives (**Fig. S2D**).

152

153 We also examined whether cells with high mitochondrial contents affect clustering of ferret
154 single cells, because we have decided to include all cells that had less than 30% of
155 mitochondrial genes in our analysis based on the percentage of reads mapped on the
156 mitochondrial genome; we found that the majority of cells in each cell type had a value less
157 than 5% while some cells contained them in the range between 0% and 10%, up to a maximum
158 of 28% (**Fig, S2B**). We comfirmed that single cells after filtering cells with the threshold of
159 10% mitochondrial content (28,686 cells in our dataset) and those with the threshold of 30%
160 (**Fig.1C**), provided a similar clustering patterns with each other, both of which 26 clusters **(Fig.**
161 **S3C)** indicating that the current selection of cells with the mitochondrial contents is appropriate.

Cell clusters were annotated according to their specific gene expression patterns (**Fig. 1D, 1E, S3A, Table S1**) and assigned into ten cell types: RG (early, mid, and late), IPC, OPC, ependymal cells, excitatory cortical neurons (DL and UL), inhibitory neurons (ITN), microglia, endothelial cells, mural cells, and unknown cells (**Fig. 1C**). RG, IPC, and neuronal clusters were aligned according to the neuronal differentiation process in the UMAP plot (**Fig. 1C**). RG cells were classified into three clusters (early, mid, and late) according to their collection stages and also the expression of temporally altered RG markers reported previously (hereafter named temporal markers) (Okamoto et al, 2016; Telley *et al*, 2019). The "early RG" clusters comprised E25 cells while the "mid RG" clusters, mostly E34 cells (**Fig. S3B**). Early and late RG, and IPC were subdivided into three subclusters that expressed different cell cycle markers (**Fig. S3D**).

Remarkably, we identified a small cluster (409 cells) of *PAX6*-expressing RG subtype, 69% of which expressed *CRYAB* (**Fig. 1F**). *CRYAB*, encoding a molecular chaperone (Yamamoto et al, 2014) is a unique marker for human tRG (Nowakowski et al, 2016); therefore, we designated them as tRG-like cells in ferrets. In contrast, oRG cells failed to be distinguished from ventricular RG cells (vRG) in ferrets by unbiased clustering alone (see below). HOPX, a typical marker for oRG in human tissues (**Fig. 1G, S3E**; Pollen et al, 2015), has been indeed detected in both oRG and vRG at late stages *in vivo* in ferrets (**Fig. S3E**; Johnson et al, 2018; Kawaue et al, 2019).

tRG emerge around birth during the development of somatosensory cortex in ferrets

The presence of a tRG-like cluster in ferret transcriptomes led us to investigate the properties of the cells in this cluster. To examine their cell morphology, we sparsely labeled NPC by electroporating P0 embryos with an expression vector for enhanced green fluorescent protein (EGFP) and found a cell population showing major characteristics of human tRG cells (Nowakowski et al, 2016): expression of CRYAB and PAX6 with an apical endfoot and truncated basal fiber in the VZ during late neurogenesis (**Fig. 2A, 2B, Supplementary movie1, 2**). CRYAB expression emerged shortly prior to birth (day 41), gradually increasing in cell number, and became mostly restricted to tRG-shaped cells in the VZ and SVZ (**Fig. 2C, 2D, S4A**). These CRYAB^{+} cells were mostly post-mitotic (KI67^{-}) and neither IPC (TBR2^{+}) nor

195 OPC (OLIG2^{+}) at P10, while a small fraction of those cells expressed these markers at P5 (**Fig.**
196 **2E–2G**). These histochemical observations were consistent with our single-cell transcriptome
197 data (**Fig. S4A–F**). Altogether, we concluded that tRG-like cells in ferrets are equivalent to
198 human tRG cells (as also confirmed by transcriptomic comparison between humans and ferrets,
199 shown later). A difference in the late neurogenic cortex between humans and ferrets is that the
200 VZ and OSVZ are connected by conventional RG cells in ferrets (**Fig. S4G**), but separated in
201 humans due to the disappearance of conventional RG cells (Nowakowski et al, 2016).
202
203 **Temporal fates of RG cells are predicted by pseudo-time trajectory analysis**
204 To understand the relationship between various cortical progenitors in the developing ferret
205 brain, particularly in the origin and fate of ferret tRG, pseudo-time trajectory analysis was
206 performed. Single cells that had been subjected to single-cell transcriptome analyses (from E25
207 to P10) were unbiasedly ordered along a trajectory based on their transcriptome profiles (**Fig.**
208 **S5A, S5B**). To simplify our analysis, we first excluded interneurons, microglia, endothelial
209 cells, and excitatory neuronal clusters. Subsequently, 6,000 single cells were randomly selected
210 from the remaining cell population for further analysis. The pseudo-time analysis predicted a
211 reasonable trajectory consisting of three branching points that generated seven states (**Fig. 3A,**
212 **S5B**). We assigned major cell types for each state based on the cell clusters defined by UMAP
213 analysis (**Fig. 1C, Table S2**). The trajectory successfully predicted cortical development in the
214 somatosensory area, along which *HES1*$^{+}$ stem cells shift their features from the earlier to the
215 later stages, generating branches of differentiated cells (**Fig. 3B, 3C, S5D**). Major *HES1*$^{+}$stem
216 cell states (state 1, 3, 5 and 7) contained cells at different stages; thus termed NPC1, 2, 3 and
217 astrogenic, respectively (**Fig. S5C**). NPC1 (mostly from E25) bifurcated into the neuronally
218 differentiated lineage and NPC2 state (**Fig. S5B**), which produced the OPC lineage and NPC3
219 state at the second branching point. When neurogenesis gradually declined after birth, the
220 NPC3 state, mainly consisting of late RG cells and tRG (**Fig. S5C**), adopted two states, state 6
221 with an ependymal fate (*FOXJ1*$^{+}$, *SPARCL1*$^{+}$, *AQP4*$^{+}$) and state 7 with astrogenic fate (*FOXJ1*$^{-}$,
222 *SPARCL1*$^{+}$, *AQP4*$^{+}$), as judged by the combination of late fate markers (Liu et al, 2022;
223 Saadoun and Papadopoulos, 2010; Yu et al, 2008, **Fig. 2A, 3D**).
224
225 Remarkably, tRG cell population was distributed into three states along the pseudo-time
226 trajectory (**Fig. 3E, 3F**): NPC3 (mainly during E40–P1), astrogenic (P1–P10), and ependymal
227 (P5–P10) states, suggesting that tRG prenatally arise as precursors of ependyma and astroglia

228 in the ferret cortex (see below). Different territories were assigned into these three states in the
229 UMAP even when we examined the entire tRG population (409 cells) before making a random
230 selection of 6,000 cells for pseudotime trajectory analysis, ensuring the reliability of this
231 categorization of tRG (**Fig. 3E**).
232

233 **tRG cells possess ependymal and gliogenic potential during cortical development in**
234 **ferrets**

235 To test the hypothesis that tRG generate both ependymal cells and astroglia populations, we
236 first examined the expression of an ependymal marker, FOXJ1, a master regulator of
237 ciliogenesis, according to CRYAB expression in the VZ. We observed that CRYAB^{+} tRG
238 cells gradually co-expressed FOXJ1, reaching up to 90% co-expression by P10 (**Fig. 4A,**
239 **4B**). Similarly, our transcriptome data showed that the fraction of *CRYAB-FOXJ1* double-
240 positive cells increased in the tRG cluster from P1 to P10, whereas other RG clusters
241 maintained low *CRYAB* expression (**Fig. 4C, 4D**). From P5 onwards, differentiating
242 ependymal cells (*CRYAB-FOXJ1* double-positive) accumulated within the VZ (**Fig. 4A**).
243 These cells often align their nuclei in parallel to the ventricular surface, near which nuclear
244 lined aggregates are observed more frequently (between two arrowheads in P5 and P10 in
245 **Fig. 4A, 4B**), and their cell body finally settled on the apical surface with short basal fibers
246 by P14 (**Fig. 4E**). These data indicate that a majority of tRG cells progressively upregulates
247 *FOXJ1* expression to adopt an ependymal cell fate during postnatal development.
248 Concomitantly, adenine cyclase III expression in both primary and multiciliated cells
249 indicated that ciliogenesis progressed postnatally, forming multi-ciliated ependymal cells on
250 the ventricular surface of the ferret cortex by P35 (**Fig. S6A**).
251

252 Moreover, a fraction of tRG belongs to the state 7 (astrogenic state) in the pseudo-time
253 trajectory (**Fig. 3E, 3F**). We examined whether these tRG cells differentiate into astrogenic
254 cells. We chose *FOXJ1* as an ependymal marker and *SPARCL1* as an early astroglial marker
255 based on a recent study in mice (Liu *et al*, 2022). While *SPARCL1* is expressed in all states
256 generated by NPC2 (**Fig. S6B**), *SPARCL1* expression is highest in astrogenic tRG among the
257 three tRG subgroups, whereas *FOXJ1* expression is nearly exclusive to ependymal tRG (**Fig.**
258 **4F**). Furthermore, cells expressing high levels of *SPARCL1* do not express *FOXJ1* (**Fig. 4G,**
259 **Table S3**). These features of the astrogenic tRG are essentially the same as those of the
260 astrogenic state (state 7) of the pseudo-time trajectory (**Fig. 3D**). Consistently, whereas

261 FOXJ1^{+} cells were located close to the apical surface, those expressing *SPARCL1* were
262 observed relatively far from the apical surface in the VZ (**Fig. 4H, 4I, S6C, Table S4**).
263 Altogether, our analyses strongly suggest that tRG cells adopt both the ependymal and
264 astrogenic fates.
265
266 **Ferrets and humans show a homologous developmental transcriptomic profile of**
267 **progenitor subtypes**
268 Both ferrets and humans are positioned in distinct phylogenetic branches; both represent
269 complex brain features of gyrencephalic mammals. Therefore, we compared our temporal
270 series of ferret single-cell transcriptomes with a previously published human dataset
271 (Nowakowski et al, 2017) to examine which processes are species-specific or common for the
272 two species. We merged the two datasets by pairing mutual nearest neighbor cells (MNN)
273 following canonical correlation analysis (CCA) across species (Stuart and Butler et al, 2019)
274 and found that many cell types, including RG, IPC, OPC, and neurons, were clustered together
275 (**Fig. 5A, 6B, S7A**). Temporal patterns and variety of neural progenitors during cortical
276 developments were similar to each other between humans and ferrets at the single cell
277 transcriptome level. Nonetheless, the timescales of cortical development significantly differed:
278 on the UMAP plot, ferret E25 cells closely distributed with human GW8 cells; ferret E34, with
279 human GW11–14; ferret E40–P1, with human GW15–16; and ferret P5–P10, with human
280 GW17–22 (**Fig. 5B**).
281
282 Next, we compared the similarities among individual RG subtypes across species. To quantify
283 the features of an RG subtype, we introduced the parameter "genescore" (Bhaduri et al, 2020),
284 which reflected the enrichment and specificity of a marker gene for a given cluster (see
285 **Materials and Methods**). Comparison of genescores of two arbitrary RG subtypes between
286 two species revealed a high correlation in the early and late RG clusters (vRG, and oRG for
287 the human dataset) across species (**Fig. 5C, 5D, Table S5**).
288
289 tRG cells also showed a remarkable similarity between the two species (**Fig. 5C, 5D**), as
290 represented by a high level of expression for the combination of *CRYAB*, *EGR1,* and *CYR61*
291 (**Fig. 5E**). To better examine this similarity, we defined the "cluster score" for individual cells
292 as a linear combination of the expression level of marker genes in a cell, which is weighted by
293 its genescore in the human cluster of interest. Calculation of the cluster score for ferret tRG

294 using genescores of the human tRG cluster resulted in a higher score than any other cluster in
295 both datasets (**Fig. 5F**). These results confirm, via transcriptomics, that the ferret tRG cluster
296 is very close to the human one.
297
298 **Transcriptional analysis of human tRG subtypes by integration with ferret tRG subtypes**
299 Next, we assessed whether human tRG cells also possessed ependymal and gliogenic potential,
300 as observed in ferret cells. We chose a recently published human dataset at GW25 (Bhaduri et
301 al, 2021) for comparison because the GW25 dataset includes more tRG cells than the previous
302 datasets. After excluding neurons and other cell types from the analysis, we identified
303 respective human clusters for tRG and oRG cells based on their marker gene expression (**Fig.**
304 **6A, Table S6).** Then, we merged human and ferret NPCs (**Fig. 6B, 6C**) as described before
305 (**Fig. 5A**). This procedure revealed that human tRG and oRG share similar transcriptomes with
306 ferret tRG and later RG, respectively (**Fig. S8A, S8B**). It is worth noting that early RG in ferrets
307 showed the highest similarity with "OLIG1" in human data, and no cell type in human data
308 corresponded to ferret "midRG," likely because only GW25 cells were used for comparison
309 (**Fig. S8B**).
310
311 The integration of ferret and human datasets showed that tRG from both species were mainly
312 distributed into three different clusters: 7, 21, and 28 (**Fig. 6F, S8C**). Cluster 7 cells highly
313 expressed late onset RG genes (such as *APOE*, *FABP7*, *NOTCH2*, and *DBI*; **Fig. S8D**),
314 suggesting that tRG cells in cluster 7 were presumably at a late RG-like state, being not yet
315 committed to neither astrogenic nor ependymal fates (mostly in the NPC 3 state in the ferret
316 pseudo-time trajectory; **Fig 3A, 3E**). In contrast, cells in clusters 21 and 28 highly expressed
317 marker genes for the astrocyte (*GFAP* and *AQP4*), and the ependymal (*FOXJ*1) clusters,
318 respectively (**Fig. S8D, Table S6**). Then, we confirmed that the three states of ferret tRG cells,
319 committed to the astroglia, ependymal fates and uncommitted states, were largely assigned to
320 clusters 21, 28 and 7, respectively (**Fig. 6G**), guaranteeing the reliability of this method. Thus,
321 our results raise the possibility that tRG cells in humans possessed the potential to generate
322 astrocytes and ependymal cells as suggested for ferret tRG. This analysis also reveals that the
323 proportion of the three subtypes of tRG was different between human and ferret datasets (**Fig.**
324 **6D–F**), possibly due to the differences in developmental stages between the two datasets in
325 terms of tRG fate, while the two presumptively committed tRG are very minor populations in
326 humans (see Discussion).

327 **Human cortical organoids lack tRG population**

328 Human cortical organoids are a powerful model for understanding cortical development
329 (Eiraku *et al*, 2008). It is, therefore, important to know how developing ferret cortices resemble
330 human cortical organoids especially regarding to features shared by human tissues and ferrets.
331 We then searched tRG cells existing two datasets for cortical organoids (Bhaduri et al., 2020;
332 Herring et al., 2022), focusing on CRYAB-expressing cells (**Fig. S8A-D**). We failed to find
333 organoid-derived CRYAB-expressing cells that overlapped with tRG cells from the human
334 primary tissues (Bhaduri et al., 2020; **Fig. S8C, D**), nor CRYAB-expressing cells present in
335 the dataset (Herring et al., 2022; **Fig. S8E**). Our analyses thus suggest that tRG-like populations
336 seem to be lacking in available organoid datasets.

337

338 **Prediction of ferret oRG-like cells via the identification of cells homologous to human**
339 **oRG cells**

340 As mentioned before, oRG could not be identified as a separate cluster in the ferret dataset (**Fig.**
341 **1**). We attempted to assign oRG-like cells in the ferret dataset using human oRG cells as
342 anchors via the integration of two datasets by the MNN after CCA (**Fig. 6B**). We could assign
343 oRG-like cells, which were located near the human oRG cluster (**Fig. 6H**). To assess the degree
344 of similarity to human oRG, we calculated the oRG score for each ferret oRG-like cell as we
345 did for tRG (**Fig. 5F**). The assigned oRG-like cells had significantly higher oRG cluster scores
346 than all other NPCs (**Fig. 6I**). Furthermore, we searched genes that were highly expressed in
347 oRG-like cells by comparing oRG-like cells and other NPCs in the ferret dataset (**Table S6**).
348 Consistent with the human dataset (Bhaduri *et al*, 2021), the expression of *HOPX, CLU,* and
349 *CRYM* was higher in oRG-like cells than in other ferret NPCs (**Fig. 6J, S9E**). However, human
350 oRG markers such as *HOPX* and *CLU* were also expressed by vRG and tRG in ferrets (**Fig.**
351 **S3D, S9F**). Therefore, oRG at the transcriptome level can only be distinguished by the
352 similarity with the whole transcriptome or a combination of several markers, but not by a few
353 marker genes.

354

355 **DISCUSSION**

356 In this study, we provide a ferret dataset of single-cell transcriptomes of neural progenitors
357 covering the entire cortical neurogenenesis and early gliogenic phase, revealing their diversity
358 and temporal patterns during cortical development. Comparison of these features between
359 ferrets and humans (Nowakowski *et al*, 2017; Bhaduri *et al*, 2021) indicated at a high resolution
360 that these two gyrencephalic mammals shared a large proportion of progenitor variations and

361 their temporal sequences despite their extremely different neurogenesis timescales. It is
362 remarkable that tRG is conserved between these two phylogenetically distant species. A ferret
363 model allowed us to identify the mode of tRG generation, to predict its descendant fates and to
364 analyze cell dynamics in tissues. These findings have not been realized by previous studies,
365 which revaluate ferrets as a valuable model species to study the neural development of
366 gyrencephalic animals. This comparison could not be performed unless genomic information,
367 especially genome-wide gene models, was greatly improved; there had been sufficient genomic
368 information accumulated for ferrets, but mainly for their coding regions. However, to carry out
369 a large scale of single cell RNA seq quantitatively with minimizing the loss of transcript species,
370 accurate 3'-UTR sequences are indispensable, because typical single cell RNAseq platforms
371 are based on oligo-dT-primed cDNA synthesis. We made tremendous efforts to get improved
372 gene models that include 3'-UTR sequences, making it possible for us to compare single cell
373 transcriptome of ferret cortical progenitors with a huge volume of single cell transcriptome
374 datasets with high qualities.
375
376 **The fate of tRG progenies**
377 Our pseudotime trajectory analyses and immunohistochemistry analyses suggested that ferret
378 tRG cells differentiate into ependymal cells and astrogenic cells. Although the number tRG
379 cells used in the trajectory analysis was limited (167 cells; **Fig. 3**), three tRG subtypes,
380 "precommitted", "ependymal" and "astrogenic" tRG, also formed three distinct territories
381 within the original tRG cluster that consisted of 409 cells on UMAP, reflecting a consistent
382 heterogeneity within tRG cluster. This mode of ependymal cell formation is likely parallel to
383 that of the bifurcation of ependymal cells and adult neural stem cells from the same progenitor
384 population in the striatum on the ventral side (Ortiz-Álvarez *et al*, 2019).
385
386 **Comparison of human with ferrets in corticogenesis**
387 Our cross-species comparative analysis predict that tRG in humans also differentiate into
388 ependymal and astroglial cells although there is no *in vivo* evidence yet (**Fig. 6E**). Furthermore,
389 the rare presence of two presumptively committed tRG subgroups in humans makes this
390 prediction tentative at present. If this prediction is the case, the uncommitted tRG fraction is
391 dominant in GW25 human brains unlike in ferret brains, suggesting that human tRG at GW25
392 progresses along the differentiation axis less than ferret tRG at P5–P10, most of which are
393 already committed to either ependymal or astrogenic states.
394 While GW25 has been almost at the latest stages experimentally available from human

395 embryonic brain tissues due to ethical reasons, Herring et al. recently reported a large dataset
396 that spans late embryonic to postnatal development in human prefrontal cortex, in which we
397 were not able to detect a tRG population nor other progenitor subtypes, as well as an ependymal
398 cell type (Herring *et al*, 2022), possibly due to regional differences in the collected samples
399 from our ferret dataset. Thus, this postnatal dataset does not seem to be appropriate to compare
400 with our ferret dataset or even human prenatal dataset (Bhaduri et al. 2021) to follow tRG
401 progenies (**Fig. S9**). More enrichment of datasets in the human lateral cortices at the
402 developmental stages after GW25 onward are necessary to examine whether our results
403 obtained from ferrets regarding tRG progeny fates can be generalized.
404

405 **Commonalities and differences among characteristics of neural progenitors between**
406 **human ferrets.**

407 In this study, our transcriptomic data supported the notion that ferrets are a good model
408 system to find mechanisms commonly (at least in both primates and carnivores) underlying the
409 cortical development in gyrencephalic mammals. At the same time, we acknowledge the
410 differences in corticogenesis between ferrets and humans. Most prominently, the time scale of
411 corticogenesis progression is greatly different between the two species, while the variety of
412 NPCs and their temporal patterns of appearances and differentiation exhibit similarities. In
413 addition, the organization of cortical scaffold seems differ from each other; in human
414 corticogenesis, two major germinal layers, the VZ and OSVZ, become segregated during the
415 expansion phase of tRG in the neurogenic stage, due to the loss of vRG, which extend from the
416 ventricular surface to the laminar surface, passing through the OSVZ (Nowakowski *et al*, 2016).
417 In contrast, ferrets maintain vRG with a long radial fiber in VZ alongside with tRG cells, even
418 beyond the expansion phase of tRG (**Figure 2A, S4G**).
419

420 **Models as human cortical development**

421 Our preliminary analysis of two datasets from human cortical organoids suggests the lack
422 of tRG-like cells and potentially their progeny cell types (**Fig. S8**, Bhaduri et al., 2020; Herring
423 et al., 2022). This situation might be improved by optimizing culture protocols. If tRG and
424 ependymal cells, one of tRG progeny, are generated in human organoids, as we found in ferrets,
425 it would represent a significant advancement in the human organoid model because ependyma
426 are a fundamental structure for ventricular formation. Further studies using human cortical
427 organoids are expected to be able to generate tRG, and to examine its progeny fates.

428 In ferrets, genetic manipulations can be achieved through *in utero* or postnatal

429 electroporation, as well as via virus-mediated transfer of DNA (Borrell, 2010; Kawasaki *et al*,
430 2012; Matsui *et al*, 2013; Tsunekawa *et al*, 2016). Thus, it is theoretically possible to disrupt
431 the *CRYAB* gene *in vivo* in ferrets to investigate its role in tRG and their progeny, including
432 ependymal cells, and track the tRG lineage. If the *CRYAB* gene is essential to form ependymal
433 layers, we will be able to explore how the ventricle contributes to cortical folding and
434 expansion. Despite extensive efforts over a year, we have thus far been unsuccessful in
435 knocking in and/or knocking out the *CRYAB* gene. Nevertheless, we anticipate that technical
436 advances will surpass our expectations, both in ferret and human organoids. Taken together,
437 these functional studies in ferrets as well as in human organoids hold promising insights into
438 the understanding of the tRG lineage and its contribution to cortical development in the near
439 future.
440
441 **MATERIALS AND METHODS**
442
443 **EXPERIMENTAL MODEL AND SUBJECT DETAILS**
444 **Ferret brain tissue samples**
445 Pregnant ferrets were purchased from Marshall BioResources. We also bred them to maintain
446 a population that is sufficient to regularly get pregnant females in the animal facility of RIKEN
447 Center for Biosystems Dynamics Research under the license given from Marshall
448 BioResources. All procedures during animal experiments were performed in accordance with
449 the legal and institutional ethical regulations of RIKEN Center for Biosystems Dynamics
450 Research.
451 Ferret pups are born at day 41 or day 42 of gestation. The day of birth was counted as postnatal
452 day 0 (P0). Ferret embryos and pups were euthanized prior to brain removal.
453 Samples used for single cell RNA-sequencing were obtained from 1 or 2 pups for each
454 developmental stage: embryonic days 25, 34 and 40 and postnatal days 1, 5 and 10. Samples
455 used for immunohistology-based quantifications were obtained from 2 or 3 pups from different
456 mothers. Samples used for a time-lapse imaging were obtained from 1 animal per experiment,
457 which is performed 4 times, independently.
458
459
460 **METHOD DETAILS**
461 **Gene model construction of the ferret genome**

462 In this study, we used a ferret genome reference with expanded reference gene annotations with
463 DDBJ (detail see below). Briefly, gene models were constructed using Chromium by tagging
464 all fragments from a long genomic DNA in a droplet, so that sequences from long genomic
465 DNAs could be successfully aligned to cover so far unconnected genomic regions in the NCBI
466 (NCBI Assembly ID: 286418 (MusPutFur1.0)) database. Detailed information after mapping
467 is listed in the Supplementary Table S1B.
468
469 RNA-seq library preparation and sequencing
470 Total RNA was extracted from the embryonic tissues (Supplementary Table S7) using the
471 RNeasy mini kit (Qiagen). Concentration and length distribution of the RNA were checked
472 with the Qubit RNA HS Assay Kit on a Qubit 2.0 Fluorometer (Thermo Fisher Scientific) and
473 the RNA 6000 Nano Kit on a 2100 Bioanalyzer (Agilent Technologies). Sequencing libraries
474 were prepared using 1 μg of total RNA with the TruSeq Stranded mRNA Sample Prep Kit
475 (Illumina) and the TruSeq single-index adaptor (Illumina), except for the sample 'gonad and
476 mesonephros' (see Supplementary Table S7) for which 500 ng of total RNA was used. The
477 RNA was fragmented at 94°C for either 8 minutes or 2 minutes, which resulted in libraries
478 with variable insert size distributions (Hara *et al*, 2015). The optimal numbers of PCR cycles
479 were pre-determined using the KAPA Real-Time Library Amplification Kit (Roche) as
480 described previously (Tanegashima *et al*, 2018). Libraries were sequenced with the Rapid Run
481 mode of HiSeq1500 (Illumina) using the HiSeq PE Rapid Cluster Kit ver. 2 (Illumina) and the
482 HiSeq Rapid SBS Kit v2-HS (Illumina) to produce paired-end reads of 127 nucleotides. Base
483 calling was performed with RTA ver. 1.18.64, and the fastq files were generated with bcl2fastq
484 ver. 1.8.4 (Illumina).
485
486 Genomic DNA extraction and Chromium genome library construction
487 Genomic DNA was extracted from a liver of an adult female ferret using the CHEF Mammalian
488 Genomic DNA Plug Kit (BioRad, Cat. No. #1703591). In brief, the liver tissue of about 50 mg
489 was homogenized in PBS (-) with a Dounce tissue grinder on ice, fixed with ethanol, and
490 subsequently embedded in low melting point agarose gel (BioRad). After the protein digestion
491 with Proteinase K (QIAGEN, Cat. No. #158920) and RNA digestion with RNase A (QIAGEN,
492 Cat. No. #158924), the gel plugs were further digested by Agarase (Life Technologies, Cat.
493 No. #EO0461). DNA was purified by the drop dialysis method using the MF-Millipore
494 Membrane Filter (Merck Millipore, Cat. No. #VCWP04700). Length distribution of the
495 genomic DNA was analyzed by pulsed-field gel electrophoresis, which exhibited an average

496 length of over 2 Mbp. The Chromium library was constructed using the Chromium Genome
497 Reagent Kit v1 Chemistry (10x Genomics, Cat No. #PN-120216), and sequencing was
498 performed with an Illumina HiSeq X to obtain paired-end 151 nt-long reads.
499
500 Genome assembly
501 De novo genome assembly using the Chromium linked-reads was performed with Supernova
502 ver. 2.0.0 (10x Genomics) with the default parameters, and the resultant sequences were output
503 with the option 'pseudohap'. Detection and masking of repetitive sequences were performed
504 using RepeatMasker ver. 4.0.7 (Smit et al, 2013-2015) with NCBI RMBlast ver. 2.6.0+ and the
505 species-specific repeat library from RepBase ver. 23.01.
506
507 Gene model construction
508 Gene models for gene expression level quantification were constructed in the three following
509 steps. First, ab initio gene prediction was performed by BRAKER ver. 2.0.5 (Hoff *et al*, 2019).
510 In this process, GeneMark-ET ver. 4.33 (Lomsadze *et al*, 2014) with the information of spliced
511 RNA-seq alignment was used for training, and AUGUSTUS ver. 3.3 (Stanke *et al*, 2008) with
512 the parameters of `UTR=on, species=human` was used for gene prediction. For the
513 abovementioned training of BRAKER, the RNA-seq reads were aligned to the repeat-masked
514 genome sequences by STAR ver. 2.5.4a (Dobin *et al*, 2013) with default parameters using the
515 entire set of RNA-seq reads of various tissue types (Supplementary Table S7). Second, the
516 information of RNA-seq alignment was directly incorporated into the gene models to improve
517 the coverage of the 3' UTR region of each gene which is not reliably predicted in ab initio gene
518 prediction. This computation was performed with HISAT2 ver. 2.1.0 (Kim *et al*, 2019) and
519 StringTie ver. 1.3.4d (Kovaka *et al*, 2019), whose output GTF file was merged with the gene
520 models produced by BRAKER using the merge function of StringTie. Finally, the existing
521 transcript sequences of MusPutFur1.0 available at NCBI RefSeq (GCF_000215625.1) was
522 incorporated into the gene models by mapping their sequences to the repeat-masked genome
523 sequences using GMAP ver. 2017-11-15 (Wu & Watanabe, 2005) with the `not report chimeric
524 alignments` option. The gene name of each locus was adopted from the annotation in RefSeq,
525 and the gene name of a newly predicted locus was assigned according to the results of a
526 BLASTX search against the UniProtKB Swiss-Prot database release 2020_01. The assignment
527 was performed only for genes with a bit score (in the abovementioned BLASTX search) of
528 greater than 60. When a locus has multiple transcripts, the one with the highest score was

529 adopted for gene naming. If a transcript estimated by ab initio prediction bridged multiple
530 genes, they were incorporated into the gene models as separate genes.
531
532 Completeness assessment of assemblies
533 To assess the continuity of the genome assembly and gene space completeness of the gene
534 models, gVolante ver. 1.2.1 (Nishimura *et al*, 2017) was used with the CEGMA ortholog search
535 pipeline and the reference orthologues gene set CVG (Hara *et al*, 2015).
536
537 ***In utero* and postnatal electroporation**
538 *In utero* electroporation (IUE) and postnatal electroporation in ferrets was performed as
539 described previously (Kawasaki *et al*, 2012; Matsui *et al*, 2013; Tsunekawa *et al*, 2016 for IUE;
540 Borrell, 2010 for postnatal electroporation) with modifications. Briefly, pregnant ferrets or
541 ferret pups were anesthetized with isoflurane at indicated stages of the development. The
542 location of lateral ventricles was visualized with transmitted light delivered through an optical
543 fiber cable. Three µl of plasmid DNA solution was injected into the lateral ventricle at indicated
544 developmental stages using an injector. Each embryo or pup was placed between the paddles
545 of electrodes, and was applied a voltage pulse of 45V at the duration from 100 msec to 900
546 msec (100,0 Pon and 1000,0 Poff) 10 times for in utero electroporation, and under the same
547 condition except a voltage of 60V for postnatal electroporation (CUY21 electroporator, Nepa
548 Gene).
549
550 **Plasmids**
551 To assure a stabilized expression of transgenes, we combined expression vectors with a
552 hyperactive piggyBac transposase system to integrate expression vectors into the genome for
553 a stable expression (Yusa *et al*, 2011). To enrich neural progenitor cell populations in "AG"
554 samples used for the single-cell transcriptome analysis, pLR5-Hes5-d2-AzamiGreen (0.5
555 µg/µl; Hes5 promoter was gifted from Kageyama Laboratory; Ohtsuka *et al*, 2006) was
556 electroporated at E30 for E40, or at E34 for postnatal samples, together with pCAX-hyPBase
557 (0.5 µg/µl). Among them, for P1 and P10 samples, pPB-LR5-mCherry (0.5 µg/µl) was also
558 included in the DNA solution.
559 To sparsely label the cell cytoplasm for detailed imaging of individual cells on vibratome-cut
560 thick cortical sections, we have used pPB-LR5-floxstop-EGFP combined with a low
561 concentration of Cre-expressing plasmid. The concentrations used for these plasmids were 0.5
562 µg/µl or 1.0 µg/µl for a GFP labeling and 1 ng/µl or 10 ng/µl of Cre-expressing plasmid for P0

563 or P5 samples, respectively (Figure 2A). For all electroporation experiments, Fast Green
564 solution (0.1 mg/ml; Wako Pure Chemical Industries) was added into the freshly prepared
565 mixture of plasmid DNA to visualize the injection.
566 For in situ hybridization probes, the PCR product was inserted into pCR-BluntII-TOPO for
567 cloning and sequencing.
568
569 **Library preparation for scRNAseq**
570 10x v2 Chromium was performed on dissociated single cells according to the manufacturer's
571 protocol.
572
573 **Single cell isolation and sorting of Azamigreen-expressing cells**
574 Cell suspension was prepared as reported previously (Wu *et al*, 2022) with modifications.
575 Brains were collected at indicated stages, transferred in the ice-cold dissection Dulbecco's
576 Modified Eagle Medium (DMEM) F12 and meninges were removed. Somatosensory area was
577 dissected from embryonic or postnatal cortices using an ophthalmic knife (15°) under a
578 dissection microscope. Sliced tissues were dissociated via enzymatic digestion with papain at
579 37°C for 30 - 45 min in ice-cold Hank's Balanced Salt Solution (HBSS) (-) with EDTA (0.1
580 M). Dissociated cells were centrifuged at 1000xg for 5 min to remove papain by washing with
581 PBS and were resuspended in 0.375% BSA/HBSS (-), or in the sorting buffer (DMEM F12 +
582 GlutamaX (Thermo Fisher); 0.1 % of Penicillin/Streptomycin (Millipore); 20 ng/ml human
583 basic FGF, Peprotech; 1xB27 RA-, Gibco) for cell sorting (see below). Homogenous cell
584 suspension filtered through 35 µm strainer (Falcon).
585 To concentrate neural progenitor cell (NPC) populations at the expense of mature neurons, two
586 methods were used for each sample, except for E25, from which cells were collected using
587 whole somatosensory area:
588 1) "T" samples: the cortical plate (CP) of cortical sections were dissected out and a part of the
589 intermediate zone (IZ) was likely to be included in the discarded region.
590 2) "AG" samples: brains collected at indicated stages were electroporated in utero by
591 azamiGreen (AG)-expression vector under the control of Hes5 promoter. The latter method
592 allows the expression of AG in only NPC by the presence of a degradation signal "d2" in the
593 vector to degrade AG protein in HES5-negative differentiating progeny. Only "AG" samples
594 were processed with cell sorting and dissociated cell obtained as described above were placed
595 in a SH800 cell sorter (SONY) to sort azamigreen-positive cells in 0.375%BSA/HBSS(-)

596 solution. Cell survival and cell number were quantified by Countess or Countess II (Invitrogen),
597 prior to an application of single cell isolation using 10x v2 Chromium kit.
598 Samples from the same developmental stage, except for P10 "T" sample, were born from the
599 same mother and were collected by applying either of above methods on the same day and
600 processed in parallel.
601
602 Library preparation and Sequencing
603 Single-cell libraries were generated according to the manufacturer's instructions. Cell
604 suspensions were diluted for an appropriate concentration to obtain 3,000 cells per channel of
605 a 10X microfluidic chip device and were then loaded on the 10X Chromium chips accordingly
606 to the manufacturer's instructions.
607 Total cDNA integrity and quality were assessed with Agilent 2100 Bioanalyzer.
608 Libraries were sequenced on the HiSeq PE Rapid Cluster Kit v2 (Illumina), or the TruSeq PE
609 Cluster Kit v3-cBot-HS, to obtain paired-end 26 nt (Read 1)-98 nt (Read 2) reads.
610
611 **Immunohistology and confocal imaging**
612 Ferret brains were removed from embryos or pups and fixed for 1 or 2 overnights, respectively,
613 in 1% paraformaldehyde (PFA) prepared in 0.1M phosphate buffer (PB, pH 7.4) at 4°C. P35
614 ferrets were transcardially perfused with cold PBS, followed by 4% PFA, under deep
615 anesthesia with isoflurane, then collected brains were post-fixed with 1% PFA. After the
616 fixation of brains or cortical tissue slices after a live imaging, they were equilibrated in 25%
617 sucrose overnight before embedding in O.C.T. compound (TissueTek, Sakura) and frozen in
618 liquid nitrogen. Frozen samples were stored at -80°C prior to a coronal sectioning using a
619 cryostat (CM3050S Leica Microsystems, 12µm sections). After equilibration at room
620 temperature, sections were washed in PBS with 0.1% Tween (PBST), followed by a treatment
621 with an antigen retrieval solution of HistoVT one (Nacalai Tesque) diluted 10 times in milliQ
622 water, at 70°C for 20 min. Sections were then blocked 1 hr at the room temperature (RT) in
623 PBS with 2% Triton-X100 and 2% normal donkey serum (Sigma), followed by an incubation
624 overnight at 4°C with primary antibody diluted in the blocking solution. After washing in PBST
625 three times, sections were treated with appropriate fluorescence-conjugated secondary
626 antibodies (1:500) along with 4',6-diamidino-2-phenylindole (DAPI, 1:1,000) for 1 hr at room
627 temperature. Sections were washed again prior to mounting with PermaFluor solution (Therma
628 Fisher Scientific).

629 Immunostaining of thick ferret brain sections (200 μm) were performed as previously reported
630 (Tsunekawa et al., 2016). Briefly, ferret brains were fixed in 1%PFA, washed in PB overnight
631 at 4°C, and embedded in 4% low-melting agarose (UltraPure LMP agarose, Thermo Fischer
632 Scientific). Embedded brains were sliced coronally at 200 μm thickness by a vibratome
633 (LinerSlicer, DOSAKA EM) on ice. Floating sections were washed three times with PBST,
634 treated with the blocking solution for 1 hour at RT and incubated with primary antibodies for
635 5 or 6 overnights at 4°C under shaking. Sections were then washed in PBST and treated with
636 secondary antibodies for 5 or 6 overnights at 4°C under shaking. After washing, we mounted
637 brain slices with CUBIC solution 2 to allow the transparency.
638 Fluorescent images were acquired using an FV1000 confocal microscope (Olympus, Japan).
639 Somatosensory cortices were captured with 20X or 100X objective lenses. When 100x
640 objective lens was used, z-stacks of confocal images were taken with an optical slice thickness
641 1.0 μm or 1.5 μm and MAX-projection images obtained by FiJi are shown.
642 All the antibodies used in this study are listed in Key Resources Table, and are used at
643 following concentrations: chicken anti-EGFP, 1:500; mouse anti-Alpha B Crystallin, 1:500;
644 Rabbit anti-FoxJ1, 1:500; goat anti-Olig2, 1:500; rat anti-Eomes, 1:500; rabbit anti-Pax6,
645 1:500; mouse anti-Pax6, 1:500; mouse anti Gfap, 1:500; rabbit anti-HopX, 1:500; rat anti-RFP,
646 1:500; goat anti-adenine cyclase III, 1:250; rat anti-Ctip2, 1:500; mouse anti-Satb2, 1:500, rat
647 anti-Ki67, 1:500.
648
649 **Probe preparation**
650 Primers for PCR targeting ferret *CLU* gene were designed with Primer3 ver 0.4.0 software.
651 Total RNA was isolated from embryonic ferret brain, collected in Trizol. cDNA was generated
652 from total RNA using the Prime Script 1st strand cDNA synthesis kit (Takara) according to the
653 manufacturer's recommended procedure. Target cDNA was inserted into pCR-TOPOII-Blunt
654 plasmid for cloning and sequencing using M13F or M13R primers. Anti-sense cRNA probes
655 were then generated by in vitro transcription using T7 promoter.
656
657 ***In situ* hybridization**
658 ISH was performed as described previously, with some modifications (Mashiko *et al*, 2012).
659 Briefly, ferret brains were perfused in 4%PFA in PBS and were fixed at 4%PFA in 0.1M PB,
660 Fixed brain were incubated in 30% sucrose/4%PFA in 0.1M PB for at least 1 day and were
661 stored at -80℃ until ISH. Frozen brains were sectioned in coronal plane at 25 μm using cryostat

662 (CM3050S Leica Microsystems). Sections on slides were post-fixed at 4% PFA in 0.1M PB
663 and treated with proteinase K (Roche). Sections were hybridized with digoxigenin (DIG)-
664 labeled probes at 72° C overnight in hybridization solution. Sections were then washed and
665 blocked with donkey serum and incubated with pre-absorbed DIG antibody, conjugated to
666 Alkaline phosphatase for 2 hours at room temperature. Color development was performed in
667 solution containing NBT/BCIP (Roche).
668
669 **QUANTIFICATION AND STATISTICAL ANALYSIS FOR scRNAseq.**
670
671 Statistical details including experimental n, statistical tests and significance are reported in
672 Figure Legends.
673
674 **Alignment and raw processing of data**
675 Fastq files were obtained from individual samples and were processed using Cell Ranger
676 pipeline v2. Alignment was done using "Cell Ranger count" function with default parameters
677 accordingly to manufacturer's instructions to map reads to the ferret reference (MPF_Kobe
678 2.0.27). The raw data for each set of cells within a sample was obtained by cellranger count
679 function and was read using Seurat "Read10X" function (Seurat v3.1.5) (Stuart *et al*, 2019),
680 creating a matrix for unique molecular identified (UMI) counts of each gene within each cell.
681
682 **Filtering and normalization**
683 Filtering and normalization were performed using Seurat (v3.1.5) (Stuart *et al*, 2019). Briefly,
684 each sample was filtered by removing low-quality cells with unique feature counts less than
685 200, and genes expressed in less than 3 cells (Seurat function "CreateSeuratObject"). Different
686 samples were then merged using the Seurat "merge" function. Merged data was further subset
687 by keeping cells with features (genes) over 200 and less than 5000. Raw UMI counts were then
688 normalized using "LogNormalize" as normalization method, which divided reads by the total
689 number of UMIs per cell, then multiplied by 10,000 (Seurat "NormalizeData" function). This
690 resulted in a total of 30,234 cells and 19,492 genes: E25 (3486 cells), E34AG (3223 cells),
691 E34T (2260 cells), E40AG (1102), E40T (1581 cells), P1AG (2681), P1T (3641), P5AG (2429),
692 P5T (2926), P10AG (3010) and P10T (3895).
693
694 **Single-cell clustering and visualization**

695 Cell clustering was employed to the entire cell population after removing low-quality cells,
696 using Seurat (v3.1.5) (Stuart *et al*, 2019). 2,000 highly variable genes were identified and used
697 for the downstream analysis using Seurat "FindVariableFeatures" function (selection.method
698 = "vst"), which allowed the calculation of average expression and dispersion for each gene.
699 Normalized data was then processed for scaling using Seurat function "Scale Data" with
700 default settings, which also allowed the regression of the batch. Principal component analysis
701 (PCA) was performed with 2,000 variable genes to reduce dimensionality of the scaled dataset
702 and 50 PCs were retained (Seurat "RunPCA" function). Clustering was then performed using
703 graph-based clustering approach ("Find Neighbors" function) using top 20 PCs, which were
704 selected based on the standard deviation of PCs on the elbowplot created by Seurat function
705 "ElbowPlot" and based on statistical significance calculated by JackStraw application. Briefly,
706 cells are embedded in a k-nearest neighbor (KNN) graph based on the Euclidean distance in a
707 PCA space. Then, this knn graph is used to group cells on a shared nearest neighbor graph
708 based on calculations of overlap between cells with similar gene expression patterns (Jaccard
709 similarity). Cells were then clustered by Louvain algorithm implemented in Seurat
710 "ClusterCells" function (resolution = 0.8, dims = 1:20). Next, we used Seurat "RunUMAP"
711 function, which resulted in cell clusters being separated in embedding space while preserving
712 the balance between local and global structure.
713
714 **Cluster annotations**
715 Cluster markers were obtained using "FindAllMarkers" Seurat function. We tested genes that
716 showed at least a 0.25-fold difference between the cells in the cluster and all remaining cells,
717 and that were detected in more than 25% of the cells in the cluster. Clusters, which we called
718 subtypes, were then annotated by comparing cluster markers to previously identified cell type
719 markers in the literature for mouse and human datasets. The full list of markers is given under
720 Table S1. The heatmap in Figure 2D shows the expression data for the top 10 highly expressed
721 marker genes for each cluster using a downsampling of maximum 500 cells from each cluster.
722 Plotting cells onto the UMAP plot by their batch indicated that batches did not influence
723 clustering (**Fig. 2C**) in accordance with the differential expression of cluster markers (Figure
724 2D, S2C). When a cluster was enriched based on the developmental stage, the information was
725 included in the annotation. For example, "early RG" cluster was enriched in E25 samples, and
726 expressed both common radial glial cell markers shared with other RG clusters in our dataset,
727 but also expressed early onset-genes reported in mouse studies (Okamoto *et al*, 2016; Telley *et*

728 *al*, 2019), such as *HMGA2*, *FLRT3*, *LRRN1* (Table S1). Therefore, we named this cluster as
729 "early RG" based on its age-dependent properties.
730 To achieve more precise clustering, cycling cells were identified with known markers
731 implemented in Seurat package (S genes and G2M genes). Clusters enriched in S genes or
732 G2M genes were identified, including early_RG2 (S), early_RG3 (G2M), late_RG2 (G2M),
733 late_RG3 (S), IPC2 (S) and IPC3 (G2M) (Figure S2B). Subtypes of RG and IPC clusters were
734 further combined to facilitate the data representation (Figure S2C-D).
735
736 **Differential gene expression analysis**
737 Differential gene expression (DEG) analysis was assessed using "FindMarkers" Seurat
738 function with default parameters.
739
740 **Pseudotime analysis**
741 Monocle 2 was used to construct developmental trajectories based on pseudotime ordering of
742 single cells (Qiu *et al*, 2017; Trapnell *et al*, 2014). We generated a subset of clusters using
743 "SubsetData" Seurat function using the raw counts. Combined progenitor clusters (F_earlyRG,
744 F_midRG, F_lateRG, F_tRG, F_IPC, F_OPC) were selected. All clusters known to be
745 generated from a non-cortical origin including microglia, endothelial and mural cells, were
746 removed prior the pseudotime analysis. The expression matrix and a metadata file that
747 contained above cluster information defined by Seurat were used as input for monocle package
748 (Table S2).
749 The "differentialGeneTest" function was used to select genes for dimensionality reduction
750 (fullModelFormulaStr = '~Subtype.combined'). Top 1,000 genes were then applied for cell
751 ordering. The visualization of the minimum spanning tree on cells was obtained by Monocle2
752 "plot_complex_cell_trajectory" function. To visualize the ordered cells on Seurat's UMAP
753 plot, we extracted the branch information for cells and added as metadata of the merged Seurat
754 object ("AddMetaData" Seurat function).
755
756 **Processing External scRNA-seq Datasets for comparisons and preprocessing**
757 scRNA-seq data of developing human brain from Nowakowski *et al*. (2017), from Bhaduri *et*
758 *al*. (2021) were used for cross-species comparisons (**Figures 5, 6, S7-S9**). All cells included in
759 the analysis and cluster assignments from the provided matrix were mapped to the cell type
760 assignments provided in the metadata of Nowakowski et al. dataset and the cell type labels
761 were used as provided by the authors without modification. For Bhaduri et al. dataset, GW25

762 sample was used for clustering by Seurat package as described above. For both, we removed
763 low quality cells and clusters annotated based on anatomical regions other than somatosensory
764 cortex, and removed cells with less than 200 features. For Bhaduri et al. dataset, we filtered to
765 cells with at least 200 features, less than 6,500 features and less than 5% mitochondrial genes.
766 This resulted in 25,485 cells from around 180,000 cells in Bhaduri et al. dataset, and in 2,673
767 cells in Nowakowski et al. dataset.
768 For organoid datasets, Herring et al. (2022) and Bhaduri et al., (2021) were used (**Figs. S8, S9**)
769 with default settings in Seurat. The data driven from organoids at 5-months, 9-months, 12-
770 months and organoids at 3-weeks, 5-weeks, 8-weeks, 10-weeks were used for Herring and
771 Bhaduri datasets, respectively.
772
773 **Integrated analysis of human and ferret scRNA-seq datasets**
774 Human datasets published by Bhaduri *et al*. (2021) and Nowakowski *et al*. (2017) were used
775 for integration analysis with our ferret dataset using Seurat canonical correlation analysis
776 (Stuart *et al*, 2019). First, a Seurat object was created for all datasets as described previously.
777 Briefly, each object was individually processed with a normalization and variable features were
778 identified. For human datasets, we excluded cells or samples obtained from anatomical regions
779 other than somatosensory cortex. Then, the integration anchors between human and ferret
780 Seurat objects were identified using "FindIntegrationAnchors" Seurat function with default
781 settings. The integration was then performed with "IntegrateData" Seurat function. Scaling,
782 PCA and UMAP dimensional reduction were performed to visualize the integration results.
783
784 **Cluster correlation analysis between ferret and human clusters.**
785 Correlation analysis was performed as described by Bhaduri *et al*. (2020), with modifications.
786 Briefly, lists of cluster marker genes obtained by "FindAllMarkers" Seurat function on
787 individual datasets were extracted prior to an integration (Table S5A), except for Nowakowski
788 et al dataset, for which the marker gene list was provided. A score based on the specificity and
789 the enrichment of cluster marker genes was generated (defined as "Genescore"). A genescore
790 value was obtained by the multiplication of the average fold change that represents the gene
791 enrichment, with the percentage of the cells expressing the marker in the cluster (pct.1) divided
792 the percentage of the cells from other clusters expressing the marker (pct.2: specificity). This
793 function was employed on the marker genes for a human subtype of interest in the space of
794 marker genes for ferret NPC (RG, IPC, OPC and EP) clusters. Genescores for both ferret and
795 human were then obtained for all markers shared between human subtype of interest (i.e. oRG)

796 and ferret NPC subtypes. We then applied cor.test function using Pearson method to estimate
797 a correlation and the significance of the correlation for the obtained genescores between ferret
798 and human samples. These resulting values were represented for NPC subtypes on heatmap
799 plots.
800
801 **Prediction of oRG-like/tRG-like cells by cross-dataset analysis.**
802 The cell type marker genes for oRG and tRG cell types were extracted from each human
803 scRNAseq datasets. To predict human oRG-like and tRG-like cells in ferret sample more
804 precisely, we removed mature neuron, microglia, and endothelia clusters, as well as clusters
805 assigned as unknown, from individual datasets for an integration between ferret and human
806 NPC clusters using Seurat package as described in the above section (Stuart *et al*, 2019). After
807 identification of anchors between human and ferret Seurat objects using
808 "FindIntegrationAnchors", we extracted the information of each pair of anchors, which
809 including one ferret and one human cell. If the human cell in the pair belongs to oRG (tRG)
810 cluster in human dataset, we consider the other ferret cell in the same pair as oRG (tRG)-like
811 cell.
812
813 **Cluster score calculation.**
814 Based on a genescore calculated for marker genes as previously described, a cell-type
815 predictive model was generated. For both datasets, our custom-made R scripts were applied to
816 generate matrices using either human oRG markers or tRG markers using our integrated
817 subsets. In the space of matrices reduced with corresponding human marker genes, a score we
818 defined as "oRG score" or "tRG score" was created by multiplying human genescore for each
819 marker genes with the expression values of these genes in all cells present in the integrated
820 subset data. The results were represented by beeswarm and boxplot.
821
822 **Evaluation of immunolabeled cell number and statistical analysis**
823 The counting frames on images of immunolabeled sections consisted of 150 µm of width
824 regions of interests (ROIs). The numbers of immunolabeled cells within selected ROIs were
825 manually counted using the "cell counter" tool of FiJi software (Schindelin *et al*, 2012). The
826 VZ was identified by its cell density visualized by DAPI, and according to its thickness
827 measured by a vertical length from the ventricular surface at indicated stages (100 µm at P5,
828 70 µm at P10). The proportions of immunolabeled cells positive for various markers were

829 calculated using the summed data counted within all ROIs. The data obtained from lateral
830 cortices of somatosensory area was averaged from 2 to 3 sections.
831 For CRYAB-positive cells, we only counted cells with nuclei which were visualized by DAPI
832 staining. The numbers of positive cells were counted using two or three different animals.
833 Quantification was followed by Wilcoxon test to assess statistical significance and data on each
834 section were considered as n = 1.
835
836 **Quantification of RNAscope in situ hybridization and immunostaining image**
837 Images of RNAscope in situ hybridization and FOXJ1 immunostaining were captured by using
838 an IX83 inverted microscope (Olympus) equipped with Dragonfly 200 confocal unit (Andor),
839 Zyla Z4.2 sCMOS camera (Andor), and UPLXAPO 60XO objective lens (Olympus). Imaging
840 was performed to satisfy Nyquist sampling (xy = 48 nm/pixel by using 2x zoom optic and z =
841 136 nm interval) and 3D deconvolution was performed by ClearView-GPU™ option of Fusion
842 software (Andor). Default deconvolution parameter is used except for number of irritation (n
843 = 24) and mounting media reflection index (RI = 1.46). For quantification of images,
844 CellProfiler version 4.2.4 (Stirling *et al*, 2021) was used. To detect mRNA dots of RNAscope
845 in situ hybridization images, a single Z section of deconvolved images were processed by
846 EnhancingSpeckles module (10 pixels size) and then mRNA dots were detected by
847 IdentifyPrimaryObjects module, adaptive Otsu two class method, using default parameter
848 except for size of adaptive window (size = 10). Dot's diameter less than 4 pixels were removed
849 as a background noise. Cytoplasmic ROIs were generated from smoothed RNAscope in situ
850 hybridization images by MedianFilter module (window size = 10) and manually drawn seed
851 ROIs of DAPI staining images by using IdentifySecondaryObjects module (propagation
852 adaptive Otsu two class method, using default parameter). FoxJ1 immunostaining raw images
853 were measured by MeasureImageIntensity module. Quantified data were visualized and
854 clustered by using RStudio (version 2022.07.1+554) with R (version 4.0.3). Each of mRNA
855 count data and protein staining intensity data was log transformed and normalized, and
856 hierarchical clustering was done by using a Euclidian distance and complete clustering method
857 and cut tree to 4 clusters. Each cluster expression was plotted and classified to single or double
858 positive, or double negative of SPARCL1 and FOXJ1 populations.
859
860 **Data and code availability**
861 Genome assembly and chromium linked-read sequences were deposited in the DDBJ under
862 accession numbers BLXN01000001–BLXN01022349 and DRA010274. The gene models are

available from Figshare under the DOI: 10.6084/m9.figshare.12807032. Single-cell RNA-seq data have been deposited in the DDBJ under the number PSUB013536.

Any information required to obtain and reanalyze the data reported in this paper is available from the lead contact upon request.

Acknowledgements

We thank Kazuaki Yamaguchi, Rohab F. Abdelhamid, and Chiharu Tanegashima for sequencing RNA and genomic DNA and all members of the Laboratory of Cell Asymmetry for providing technical support and helpful discussions. We also thank an anonymous reviewer 1 of Review Commons for his/her constructive suggestions. This work was supported by JSPS KAKENHI [Grant Numbers 18H04003, 17H05779, 19H04791] and RIKEN. RIKEN funds F.M. M.B. was a RIKEN International Program Associate. Q.W. was supported by a JSPS Postdoctoral Fellowship and a RIKEN Special Postdoctoral Researcher Program.

Author contributions

M.B., Q.W., and F.M. designed experiments. M.K., O.N., Q.W., Y.K., and S.K. constructed new ferret gene models. M.B. and Q.W. performed scRNA-seq experiments and bioinformatics analyses. M.B., Y.T., and Q.W. performed molecular biological analyses. M.B., T.S. [Taeko] and T.S. [Tomomi] performed histological analyses. A.S and Q.W. performed and analyzed RNA/protein double-tissue staining. T.S. [Taeko] carried out time-lapse imaging. T.S. [Taeko], Y.T. and H.K. bred the ferrets. M.B., Q.W., A.S. and F.M. wrote the manuscript. All authors read and approved the final manuscript for submission.

Competing interests statement

The authors declare no competing interests.

References

Bhaduri A, Andrews MG, Mancia Leon W, Jung D, Shin D, Allen D, Jung D, Schmunk G, Haeussler M, Salma J, *et al* (2020) Cell stress in cortical organoids impairs molecular subtype specification. *Nature* 578(7793): 142–148

Bhaduri A, Sandoval-Espinosa C, Otero-Garcia M, Oh I, Yin R, Eze UC, Nowakowski TJ & Kriegstein AR (2021) An atlas of cortical arealization identifies dynamic molecular

898 signatures. *Nature* 598(7879): 200–204
899 Borrell V (2010) In vivo gene delivery to the postnatal ferret cerebral cortex by DNA
900 electroporation. *J Neurosci Methods* 186: 186–195
901 Capecchi MR & Pozner A (2015) ASPM regulates symmetric stem cell division by tuning
902 Cyclin E ubiquitination. *Nat Commun* 6:8763
903 Chapman B & Stryker MP (1992) Origin of orientation tuning in the visual cortex. *Curr Opin*
904 *Neurobiol* 2: 498–501
905 Chenn A & McConnell SK (1995) Cleavage orientation and the asymmetric inheritance of
906 Notch1 immunoreactivity in mammalian neurogenesis. *Cell* 82: 631–641
907 DeAzevedo LC, Fallet C, Moura-Neto V, Daumas-Duport C, Hedin-Pereira C & Lent R
908 (2003) Cortical radial glial cells in human fetuses: Depth-correlated transformation into
909 astrocytes. *J Neurobiol* 55(3): 288–298
910 Dobin A, Davis CA, Schlesinger F, Drenkow J, Zaleski C, Jha S, Batut P, Chaisson M &
911 Gingeras TR (2013) STAR: ultrafast universal RNA-seq aligner. *Bioinformatics* 29: 15–
912 21
913 Eiraku M, Watanabe K, Matsuo-Takasaki M, Kawada M, Yonemura S, Matsumura M,
914 Wataya T, Nishiyama A, Muguruma K & Sasai Y (2008) Self-organized formation of
915 polarized cortical tissues from ESCs and its active manipulation by extrinsic signals.
916 *Cell Stem Cell* 3: 519–532
917 Fietz SA, Kelava I, Vogt J, Wilsch-Bräuninger M, Stenzel D, Fish JL, Corbeil D, Riehn A,
918 Distler W, Nitsch R, *et al* (2010) OSVZ progenitors of human and ferret neocortex are
919 epithelial-like and expand by integrin signaling. *Nat Neurosci* 13(6): 690–699
920 Fujimori A, Itoh K, Goto S, Hirakawa H, Wang B, Kokubo T, Kito S, Tsukamoto S &
921 Fushiki S (2014) Disruption of Aspm causes microcephaly with abnormal neuronal
922 differentiation. *Brain Dev* 36(8): 661–669
923 Gertz CC & Kriegstein AR (2015) Neuronal Migration Dynamics in the Developing Ferret
924 Cortex. *J Neurosci* 35: 14307–14315
925 Hansen D V., Lui JH, Parker PRL & Kriegstein AR (2010) Neurogenic radial glia in the
926 outer subventricular zone of human neocortex. *Nature* 464(7288): 554–561
927 Hara Y, Tatsumi K, Yoshida M, Kajikawa E, Kiyonari H & Kuraku S (2015) Optimizing and
928 benchmarking de novo transcriptome sequencing: From library preparation to assembly
929 evaluation. *BMC Genomics* 16: 1–12
930 Herring CA, Simmons RK, Freytag S, Poppe D, Moffet JJD, Pflueger J, Buckberry S,
931 Vargas-Landin DB, Clément O, Echeverría EG, *et al* (2022) Human prefrontal cortex
932 gene regulatory dynamics from gestation to adulthood at single-cell resolution. *Cell* 185:
933 4428-4447.e28
934 Hoff KJ, Lomsadze A, Borodovsky M & Stanke M (2019) Whole-Genome Annotation with
935 BRAKER. *Methods Mol Biol* 1962: 65–95
936 Huang W, Bhaduri A, Velmeshev D, Wang S, Wang L, Rottkamp CA, Alvarez-Buylla A,
937 Rowitch DH & Kriegstein AR (2020) Origins and Proliferative States of Human
938 Oligodendrocyte Precursor Cells. *Cell* 182(3): 594-608.e11
939 Jackson CA, Peduzzi d. J & Hickey TL (1989) Visual cortex development in the ferret. I.
940 Genesis and migration of visual cortical neurons. *J Neurosci* 9: 1242–1253
941 Jayaraman D, Kodani A, Gonzalez DM, Mancias JD, Mochida GH, Vagnoni C, Johnson J,
942 Krogan N, Harper JW, Reiter JF, *et al* (2016) Microcephaly Proteins Wdr62 and Aspm
943 Define a Mother Centriole Complex Regulating Centriole Biogenesis, Apical Complex,
944 and Cell Fate. *Neuron* 92(4): 813–828
945 Johnson MB, Sun X, Kodani A, Borges-Monroy R, Girskis KM, Ryu SC, Wang PP, Patel K,
946 Gonzalez DiM, Woo YM, *et al* (2018) Aspm knockout ferret reveals an evolutionary
947 mechanism governing cerebral cortical size. *Nat 2018 5567701* 556: 370–375

Johnson MB, Wang PP, Atabay KD, Murphy EA, Doan RN, Hecht JL & Walsh CA (2015) Single-cell analysis reveals transcriptional heterogeneity of neural progenitors in human cortex. *Nat Neurosci* 18(5): 637–646

de Juan Romero C, Bruder C, Tomasello U, Sanz-Anquela JM & Borrell V (2015) Discrete domains of gene expression in germinal layers distinguish the development of gyrencephaly. *EMBO J* 34(14): 1859–1874

Kawasaki H, Iwai L & Tanno K (2012) Rapid and efficient genetic manipulation of gyrencephalic carnivores using in utero electroporation. *Mol Brain* 5:24

Kawaue T, Shitamukai A, Nagasaka A, Tsunekawa Y, Shinoda T, Saito K, Terada R, Bilgic M, Miyata T, Matsuzaki F, *et al* (2019) Lzts1 controls both neuronal delamination and outer radial glial-like cell generation during mammalian cerebral development. *Nat Commun* 10(1):2780

Kessaris N, Fogarty M, Iannarelli P, Grist M, Wegner M & Richardson WD (2006) Competing waves of oligodendrocytes in the forebrain and postnatal elimination of an embryonic lineage. *Nat Neurosci 2005 92* 9: 173–179

Kim D, Paggi JM, Park C, Bennett C & Salzberg SL (2019) Graph-based genome alignment and genotyping with HISAT2 and HISAT-genotype. *Nat Biotechnol 2019 378* 37: 907–915

Kou Z, Wu Q, Kou X, Yin C, Wang H, Zuo Z, Zhuo Y, Chen A, Gao S & Wang X (2015) CRISPR/Cas9-mediated genome engineering of the ferret. *Cell Res* 25(12): 1372–1375

Kovaka S, Zimin A V., Pertea GM, Razaghi R, Salzberg SL & Pertea M (2019) Transcriptome assembly from long-read RNA-seq alignments with StringTie2. *Genome Biol* 20: 1–13

Liu J, Liu W, Yang L, Wu Q, Zhang H, Fang A, Li L, Xu X, Sun L, Zhang J, *et al* (2017) The Primate-Specific Gene TMEM14B Marks Outer Radial Glia Cells and Promotes Cortical Expansion and Folding. *Cell Stem Cell* 21(5): 635-649.e8

Liu J, Wu X & Lu Q (2022) Molecular divergence of mammalian astrocyte progenitor cells at early gliogenesis. *Development* 149(5): de

Lomsadze A, Burns PD & Borodovsky M (2014) Integration of mapped RNA-Seq reads into automatic training of eukaryotic gene finding algorithm. *Nucleic Acids Res* 42

Mashiko H, Yoshida AC, Kikuchi SS, Niimi K, Takahashi E, Aruga J, Okano H & Shimogori T (2012) Comparative Anatomy of Marmoset and Mouse Cortex from Genomic Expression. *J Neurosci* 32: 5039–5053

Matsui A, May T, C. YA, S. KS, Mami U, Masaharu O & Tomomi S (2013) BTBD3 Controls Dendrite Orientation Toward Active Axons in Mammalian Neocortex. *Science (80-)* 342(6162): 1114–1118

McConnell SK (1988) Fates of visual cortical neurons in the ferret after isochronic and heterochronic transplantation. *J Neurosci* 8: 945–974

McConnell SK (1995) Constructing the cerebral cortex: Neurogenesis and fate determination. *Neuron* 15: 761–768

McInnes L, Healy J & Melville J (2018) UMAP: Uniform Manifold Approximation and Projection for Dimension Reduction. *arXiv* doi: 1802.

Nishimura O, Hara Y & Kuraku S (2017) gVolante for standardizing completeness assessment of genome and transcriptome assemblies. *Bioinformatics* 33: 3635–3637

Noctor SC, Scholnicoff NJ & Juliano SL (1997) Histogenesis of Ferret Somatosensory Cortex. *J Comp Neurol* 387: 179–193

Nowakowski TJ, Bhaduri A, Pollen AA, Alvarado B, Mostajo-Radji MA, Di Lullo E, Haeussler M, Sandoval-Espinosa C, Liu SJ, Velmeshev D, *et al* (2017) Spatiotemporal gene expression trajectories reveal developmental hierarchies of the human cortex. *Science (80-)* 358(6368): 1318–1323

Nowakowski TJ, Pollen AA, Sandoval-Espinosa C & Kriegstein AR (2016) Transformation of the Radial Glia Scaffold Demarcates Two Stages of Human Cerebral Cortex Development. *Neuron* 91(6): 1219–1227

Ohtsuka T, Imayoshi I, Shimojo H, Nishi E, Kageyama R & McConnell SK (2006) Visualization of embryonic neural stem cells using Hes promoters in transgenic mice. *Mol Cell Neurosci* 31(1): 109–122

Okamoto M, Miyata T, Konno D, Ueda HR, Kasukawa T, Hashimoto M, Matsuzaki F & Kawaguchi A (2016) Cell-cycle-independent transitions in temporal identity of mammalian neural progenitor cells. *Nat Commun* 7:11349

Ortiz-Álvarez G, Daclin M, Shihavuddin A, Lansade P, Fortoul A, Faucourt M, Clavreul S, Lalioti ME, Taraviras S, Hippenmeyer S, *et al* (2019) Adult Neural Stem Cells and Multiciliated Ependymal Cells Share a Common Lineage Regulated by the Geminin Family Members. *Neuron* 102(1): 159-172.e7

Polioudakis D, de la Torre-Ubieta L, Langerman J, Elkins AG, Shi X, Stein JL, Vuong CK, Nichterwitz S, Gevorgian M, Opland CK, *et al* (2019) A Single-Cell Transcriptomic Atlas of Human Neocortical Development during Mid-gestation. *Neuron* 103(5): 785-801.e8

Pollen AA, Nowakowski TJ, Chen J, Retallack H, Sandoval-Espinosa C, Nicholas CR, Shuga J, Liu SJ, Oldham MC, Diaz A, *et al* (2015) Molecular Identity of Human Outer Radial Glia during Cortical Development. *Cell* 163(1): 55–67

Pulvers JN, Bryk J, Fish JL, Wilsch-Bräuninger M, Arai Y, Schreier D, Naumann R, Helppi J, Habermann B, Vogt J, *et al* (2010) Mutations in mouse Aspm (abnormal spindle-like microcephaly associated) cause not only microcephaly but also major defects in the germline. *Proc Natl Acad Sci U S A* 107(38): 16595–16600

Qiu X, Mao Q, Tang Y, Wang L, Chawla R, Pliner HA & Trapnell C (2017) Reversed graph embedding resolves complex single-cell trajectories. *Nat Methods* 14: 979–982

Rash BG, Duque A, Morozov YM, Arellano JI, Micali N & Rakic P (2019a) Gliogenesis in the outer subventricular zone promotes enlargement and gyrification of the primate cerebrum. *Proc Natl Acad Sci* 116(14): 7089 LP – 7094

Rash BG, Duque A, Morozov YM, Arellano JI, Micali N & Rakic P (2019b) Gliogenesis in the outer subventricular zone promotes enlargement and gyrification of the primate cerebrum. *Proc Natl Acad Sci* 116(14)

Reillo I & Borrell V (2012) Germinal Zones in the Developing Cerebral Cortex of Ferret: Ontogeny, Cell Cycle Kinetics, and Diversity of Progenitors. *Cereb Cortex* 22: 2039–2054

Reillo I, De Juan Romero C, García-Cabezas MÁ & Borrell V (2011) A role for intermediate radial glia in the tangential expansion of the mammalian cerebral cortex. *Cereb Cortex* 21: 1674–1694

Rowitch DH & Kriegstein AR (2010) Developmental genetics of vertebrate glial–cell specification. *Nature* 468(7321): 214–222

Saadoun S & Papadopoulos MC (2010) Aquaporin-4 in brain and spinal cord oedema. *Neuroscience* 168(4): 1036–1046

Schindelin J, Arganda-Carreras I, Frise E, Kaynig V, Longair M, Pietzsch T, Preibisch S, Rueden C, Saalfeld S, Schmid B, *et al* (2012) Fiji: an open-source platform for biological-image analysis. *Nat Methods 2012 97* 9: 676–682

Shitamukai A, Konno D & Matsuzaki F (2011) Oblique radial glial divisions in the developing mouse neocortex induce self-renewing progenitors outside the germinal zone that resemble primate outer subventricular zone progenitors. *J Neurosci* 31: 3683–3695

Sidman RL & Rakic P (1973) Neuronal migration, with special reference to developing human brain: a review. *Brain Res* 62(1): 1–35

1048 Smart IHM, Dehay C, Giroud P, Berland M & Kennedy H (2002) Unique Morphological
1049 Features of the Proliferative Zones and Postmitotic Compartments of the Neural
1050 Epithelium Giving Rise to Striate and Extrastriate Cortex in the Monkey. *Cereb Cortex*
1051 12(1): 37–53
1052 Stanke M, Diekhans M, Baertsch R & Haussler D (2008) Using native and syntenically
1053 mapped cDNA alignments to improve de novo gene finding. *Bioinformatics* 24: 637–
1054 644
1055 Stirling DR, Swain-Bowden MJ, Lucas AM, Carpenter AE, Cimini BA & Goodman A
1056 (2021) CellProfiler 4: improvements in speed, utility and usability. *BMC Bioinformatics*
1057 22
1058 Stuart T, Butler A, Hoffman P, Hafemeister C, Papalexi E, Mauck WM, Hao Y, Stoeckius M,
1059 Smibert P & Satija R (2019) Comprehensive Integration of Single-Cell Data. *Cell*
1060 177(7): 1888-1902.e21
1061 Tanegashima C, Nishimura O, Motone F, Tatsumi K, Kadota M & Kuraku S (2018)
1062 Embryonic transcriptome sequencing of the ocellate spot skate Okamejei kenojei. *Sci*
1063 *Data 2018 51* 5: 1–6
1064 Telley L, Agirman G, Prados J, Amberg N, Fièvre S, Oberst P, Bartolini G, Vitali I, Cadilhac
1065 C, Hippenmeyer S, *et al* (2019) Temporal patterning of apical progenitors and their
1066 daughter neurons in the developing neocortex. *Science* 364
1067 Trapnell C, Cacchiarelli D, Grimsby J, Pokharel P, Li S, Morse M, Lennon NJ, Livak KJ,
1068 Mikkelsen TS & Rinn JL (2014) The dynamics and regulators of cell fate decisions are
1069 revealed by pseudotemporal ordering of single cells. *Nat Biotechnol* 32(4): 381–386
1070 Tsunekawa Y, Terhune RK, Fujita I, Shitamukai A, Suetsugu T & Matsuzaki F (2016)
1071 Developing a de novo targeted knock-in method based on in utero electroporation into
1072 the mammalian brain. *Development* 143(17): 3216–3222
1073 Wu Q, Shichino Y, Abe T, Suetsugu T, Omori A, Kiyonari H, Iwasaki S & Matsuzaki F
1074 (2022) Selective translation of epigenetic modifiers affects the temporal pattern and
1075 differentiation of neural stem cells. *Nat Commun 2022 131* 13: 1–18
1076 Wu TD & Watanabe CK (2005) GMAP: a genomic mapping and alignment program for
1077 mRNA and EST sequences. *Bioinformatics* 21: 1859–1875
1078 Yamamoto S, Yamashita A, Arakaki N, Nemoto H & Yamazaki T (2014) Prevention of
1079 aberrant protein aggregation by anchoring the molecular chaperone αB-crystallin to the
1080 endoplasmic reticulum. *Biochem Biophys Res Commun* 455: 241–245
1081 Yu X, Ng CP, Habacher H & Roy S (2008) Foxj1 transcription factors are master regulators
1082 of the motile ciliogenic program. *Nat Genet* 40(12): 1445–1453
1083 Yusa K, Zhou L, Li MA, Bradley A & Craig NL (2011) A hyperactive piggyBac transposase
1084 for mammalian applications. *Proc Natl Acad Sci U S A* 108: 1531–1536
1085 Zheng K, Wang C, Yang J, Huang H, Zhao X, Zhang Z & Qiu M (2018) Molecular and
1086 Genetic Evidence for the PDGFRα-Independent Population of Oligodendrocyte
1087 Progenitor Cells in the Developing Mouse Brain. *J Neurosci* 38: 9505–9513
1088 Zhong S, Zhang S, Fan X, Wu Q, Yan L, Dong J, Zhang H, Li L, Sun L, Pan N, *et al* (2018)
1089 A single-cell RNA-seq survey of the developmental landscape of the human prefrontal
1090 cortex. *Nature* 555(7697): 524–528
1091 Smit, AFA, Hubley, R & Green, P. (2013-2015) *RepeatMasker Open-4.0*. Available at:
1092 http://www.repeatmasker.org.

1093 **FIGURE LEGENDS**

1094

1095 **Figure 1 - Single-cell RNA-seq reveals ferret transcriptome signatures and the cell types.**
1096 **A** Schematic representing cortical development and emergence of diverse neural progenitors
1097 in humans and ferrets. Progenitors sequentially generate DL- and subsequent UL-neurons, and
1098 finally glial cells, and form ependymal cells. RG and oRG have been morphologically and
1099 positionally identified in both humans and ferrets while tRG have been only reported in humans.
1100 VZ, ventricular zone; ISVZ, inner subventricular zone; OSVZ, outer subventricular zone; IZ,
1101 intermediate zone; DL, deep layer; UL, upper layer; CP, cortical plate; NEP cell,
1102 neuroepithelial cell; Mn, migrating neuron; and EP cell, ependymal cell.
1103 **B** Schematic representing the experimental design and time points used to build the
1104 transcriptome atlas of developing somatosensory cortex of ferrets. Single cells were isolated
1105 using 10X Chromium (see Materials and Methods).
1106 **C** UMAP visualization showing cells colored by Seurat clusters and annotated by cell types
1107 (as shown in **C, D**).
1108 **D** Heatmap showing expression profiles of cluster marker genes based on log fold-change
1109 values. Cells were grouped by Seurat clustering (transverse). Cell types were assigned
1110 according to the expression of marker and differentially expressed genes in each cluster. Early
1111 RG was defined by the expression of *HMGA2, LDHA,* and *LIX1*; and late RG, by *PTN, ALDOC,*
1112 and *FABP7*. OPC, oligodendrocyte precursor cell; ITN, interneuron; and EN, endothelial cells.
1113 Other cell type abbreviations are shown in (A) and the main text. Color bar matches the Seurat
1114 clusters in (**C**). The ten most enriched representative genes in each cluster are shown, with
1115 typical marker genes noted in (**E**–**G**).
1116 **E** Normalized expression levels of representative marker genes of different cell types projected
1117 onto the UMAP plot in (**C**). MG, microglia.
1118 **F** Expression pattern of *CRYAB*, a marker for tRG, only described in humans and other primates.
1119 G The expression pattern of *HOPX*, a marker for oRG in humans and other primates in the
1120 UMAP plot.

1121

1122 **Figure 2 - Truncated tRG emerges during postnatal cortical development in ferrets.**
1123 **A** Representative images showing the cellular features of tRG and aRG in VZ at P0, and P5,
1124 respectively, stained for GFP (red) and CRYAB (green). RG cells were sparsely labelled with
1125 a GFP-expressing plasmid at E30 via IUE for P0 samples, and at P3 for P5 samples. MAX

1126 projection was performed on a 30 μm vibratome section with 5 μm or 2.5 μm interval for each
1127 z-image at P0 or P5, respectively. Scale bar, 50 μm.
1128 **B** Expression patterns of CRYAB (green) and PAX6 (red) in ferret germinal zones during
1129 postnatal development (P1, P5, and P10) (cryosection thickness = 12 μm).
1130 **C** Developmental profile of CRYAB expression in ferret cortices. Immunostaining for CRYAB
1131 (green) and DAPI (gray) on cryosections at E32, E38, P3, P5, and P10 (cryosection thickness
1132 = 12 μm).
1133 **D** Quantification of $CRYAB^+$ cells among all nuclei (DAPI) in VZ strips through
1134 immunostaining, indicating a great increase in CRYAB-expressing cells (strip width = 150 μm;
1135 n = 3 for P5; n = 2 for P10; Wilcoxon rank-sum test *p*-value = 6.574e-08).
1136 **E–G** Expression of other markers in $CRYAB^+$ cells. Representative images taken with a 100X-
1137 objective are shown with MAX projection. The border of VZ is shown with a white line. Below
1138 each double staining image, quantification of KI67-, TBR2-, or OLIG2-expressing cells among
1139 the $CRYAB^+$ cell population in the VZ is shown (n = 2 for P5; n = 2 for P10 for each staining
1140 except n = 3 for TBR2 staining). Box and whisker plots indicate ranges (lines) and upper and
1141 lower quartiles (box) with the median. Scale bars, 20 μm.
1142
1143
1144 **Figure 3 - Temporal fates of RG cells predicted by pseudo-time trajectory analysis.**
1145 **A** Pseudo-time trajectory tree of progenitor cells in the ferret developing cortex (assembled
1146 with Monocle v2). Cellular distribution at each state is the same as in the UMAP plot shown
1147 in Fig. 1C. Cell types representing each state and their gene markers are shown next to each
1148 state (see below).
1149 **B** Trajectory trees split by collection stages (AG samples are shown).
1150 **C** Distribution of cells expressing marker genes for stem cell states (*HES1* and *HMGA2*) and
1151 the neurogenic state (*EOMES*) along trajectories. Color densities indicate the log-normalized
1152 unique molecular identifier count for each gene.
1153 **D** Normalized expression of three genes: *SPARCL1, CRYAB,* and *FOXJ1* in the state 6 and
1154 state 7 cells in the pseudotime trajectory tree (Fig. 3A). The combination of expression levels
1155 of the four markers gene discriminates state 6 (ependymal) and state 7 (astrogenic). See the
1156 text for details.

1157 **E** Distribution of tRG cells along the tree and tRG-focused UMAP visualization. The tRG cells
1158 (n = 162) were found on the three states, NPC3 (9.3%; 15 cells), ependymal-tRG (61.1%; 99
1159 cells), and astrogenic-tRG (29.6%; 48 cells).
1160 **F** Composition of the three types of tRG in (D) by the collection stage (AG and T samples are
1161 combined). No tRG cells were collected from E25 and E34.
1162
1163 **Figure 4 - tRG adopt both ependymal cells and astrogenic fates in ferrets.**
1164 **A** Immunostaining of 12 µm cortical cryosections with CRYAB (green) and FOXJ1 (red),
1165 focusing on the VZ at E40, P3, P5, P10, P14, and P35. Scale bar, 50 µm. CRYAB and FOXJ1
1166 double positive nuclear rows are shown with arrowheads at P5 and P10 when this nuclear
1167 alignment is visible.
1168 **B** Percentage of FOXJ1 expression in CRYAB-expressing cells (n = 3 for P5; n = 2 for P10;
1169 Wilcoxon rank sum test *p*-value = 1.749e-05). Images with merged channels in A are shown
1170 with the same color codes, antibodies and scale bars as A.
1171 **C** Number of cells expressing both *CRYAB* and *FOXJ1* in the mid and late RG, or tRG clusters
1172 shown in Fig. 1C (with unique molecular identifier counts higher than 0.25). Colored bars
1173 indicate the stages of sample collection. *CRYAB*- and *FOXJ1*-expressing cells increased over
1174 time only in the tRG cluster.
1175 **D** Normalized expression levels of *FOXJ1* in each cell in the indicated ferret clusters in Fig.
1176 1C.
1177 **E** Cortical origin and shape of FOXJ1-expressing ependymal cells indicated with white arrows.
1178 Staining for FOXJ1 at P14 after labeling cortical progenitors with an mCherry-expressing
1179 vector via IUE at E30. The maximum projection images with 1 µm z-step size are shown.
1180 Cryosection thickness = 12 µm; scale bar = 20 µm.
1181 **F** Normalized expression of *SPARCL1* and *FOXJ1* in each cell in ferret tRG clusters separated
1182 by the pseudo-time trajectory analysis (see Table S3).
1183 **G** Relationship between *SPARCL1* and *FOXJ1* transcripts in individual cells within each tRG
1184 cluster. Within the 15 cells that were classified in state 5 tRG, only one expressed *FOXJ1*
1185 mRNA. Pearson relationship analysis was performed using cells from state 6 and 7 (R=0.19 p
1186 value=0.018).
1187 **H** Immunostaining of a P10 cortical tissue for FOXJ1 protein and S*PARCL1* mRNA.
1188 **I** Cells within the VZ in (**H**) were clustered into four classes by FOXJ1 protein± and S*PARCL1*
1189 mRNA±. Cluster A: S*PARCL1*/FOXJ1-/-, B: S*PARCL1*/FOXJ1 +/-, C: S*PARCL1*/FOXJ1-/+,

1190 D: S*PARCL1*/ FOXJ1 +/+ (Fig. S5C, S5D, Table S4). See **Materials and Methods** for
1191 clustering. Scale bar = 20 μm.
1192
1193 **Figure 5 − Comparison of molecular identity of RG subtypes between ferret and human.**
1194 **A** UMAP visualization of integrated human (n = 2,672; left) and ferret (n=30,234; right) single-
1195 cell datasets colored according to the different clusters. The names of clusters from human and
1196 ferret cells begin with "H" and "F," respectively.
1197 **B** Homologous temporal pattern of transcriptomic characters of progenitors and their progenies
1198 between ferrets and humans. Corresponding neurogenic stages between ferrets and humans can
1199 be assigned by cell distribution at homologous positions in UMAP plots. Gliogenic RG cells
1200 (a subtype of the "late_RG" group and OPC in Figure 1**B**) were first distinguished
1201 transcriptionally at ferret E40 and at human GW14, as pointed out by arrows.
1202 **C, D** Correlation coefficient (**C**) and significance (**D**) between indicated clusters of ferrets and
1203 humans, calculated by marker gene scores.
1204 **E** Normalized expression levels of the indicated genes in humans and ferrets from each
1205 progenitor cluster.
1206 **F** tRG scores of the indicated clusters are presented as box and whisker plots for humans and
1207 ferrets. These represent the range without outliers (lines) and upper and lower quartiles with
1208 the median (box). Outliers are represented as points outside the box. Outliers are 1.5-fold larger
1209 or smaller than interquartile range from the third or first quartile, respectively.
1210
1211 **Figure 6 - Identification of tRG subtypes in humans and oRG in ferrets.**
1212 **A** UMAP visualization of human brain cells colored by cell type and identified by marker genes
1213 (data from Bhaduri et al, 2021).
1214 **B** Schematic of the integration strategy of human and ferret subtypes.
1215 **C** UMAP visualization of integrated ferret and human datasets colored by different clusters.
1216 **D, E** Identification of three tRG subtypes in ferrets (D) and humans (E). The red dots highlight
1217 the indicated tRG subtypes named after pseudotime trajectory analysis in Fig. 3.
1218 **F** Distribution of humans (left) and ferrets (right) tRG in the integrated dataset. Human and
1219 ferret tRG were identified from the separated dataset.
1220 **G** Distribution of ferret tRG subtypes (identified by the pseudo-time analysis) in the integrated
1221 dataset.

1222 **H** Identification of oRG-like cells in ferret (left) and oRG cells in human (right), all highlighted
1223 as red dots.
1224 **I** oRG scores for oRG-like cells and other NPCs in ferrets. Box and whisker plots indicate
1225 ranges (lines) and upper and lower quartiles with the median (box).
1226 **J** The expression levels of *CRYM*, *CLU*, and *HOPX* in oRG-like cells and other NPCs in ferrets.
1227

1228 **Supplementary Figure Legends**

1229

1230 **Figure S1 - Temporal pattern of neurogenesis and gliogenesis in the cerebral cortex of**
1231 **ferrets.**

1232 **A.** Coronal section of the dorsal cortices immunostained for RG (PAX6, red), IPC (TBR2,
1233 green), and OPC (OLIG2, cyan) from early to late neurogenesis at E25, E32, E36, E40, P5,
1234 and P10. Scale bars = 100 μm. The position of the image strip at each stage is shown in the
1235 corresponding dorsal hemisphere image above the strip. The approximative boundaries of
1236 dorsal cortex area used for single-cell RNA sequencing are highlighted with dotty line
1237 segments in the dorsal cortex hemisphere above each strip.

1238 **B.** Immunostaining for CTIP2 (green) and SATB2 (red) at the same developmental stages as
1239 in (**A**), showing the onset of DL- (E25 or earlier) and UL-neurogenesis (E32–E34). Scale bars
1240 = 100 μm.

1241 **C.** Immunostaining for GFAP, a marker showing gliogenic potential, in cortical germinal
1242 layers at E32, E36, E40, P5, and P10. Gliogenic progenitors emerge around E40, while mature
1243 astrocytes with a typical astrocytic morphology appear later at approximately P10 onward in
1244 the outside of the germinal layers (Reillo & Borrell, 2012).

1245 **D, E.** mCherry labeling of the dorsal cortex at E30 showing that a population of OLIG2^{+}
1246 oligodendrocyte precursors are generated in the cerebral cortex by P10.

1247 **E.** As reported for both mice and humans (Zheng *et al*, 2018; Rash *et al*, 2019b; Huang *et al*,
1248 2020; Kessaris *et al*, 2006). Arrowheads in the cropped images of the left panels (E area in Fig.
1249 S1**D**) indicate cells that co-express mCherry, PAX6, and OLIG2 in the OSVZ. Scale bars = 20
1250 μm.

1251

1252 **Figure S2 - Quality-control metrics for the single cell RNA sequencing dataset.**

1253 **A.** The brain region used for the cellular isolation for a scRNA-seq are shown. Dotty lines
1254 indicate the approximative boundaries where the cut was made to obtain the cortical slices.

1255 **B.** Violin plots showing the number of genes, mRNAs and the percentage of mitochondrial
1256 genes per cell in each sample and time point.

1257 C. Table comparing quality-control metrics of an alignment with either MusPutFur 1.0 (UCSC
1258 gene models) or MusPutFur 2.60 (this study) using E34 samples. The total number of genes
1259 detected and median genes per cell were higher with MusPutFur 2.60.

1260 **D.** Separate UMAP plots for each cell collection series that was prepared by different methods,
1261 after merged clustering. Left is "AG" sample: FACS-based sorting of the neural stem cell

1262 fraction labeled with an AzamiGreen (AG)-driven *HES5* promoter (Ohtsuka et al, 2006), right
1263 is "T" samples: cells forming the VZ, SVZ, and intermediate zones (IZ) of cerebral cortices
1264 after discarding the cortical plate. E25 cells, which were mostly RG, were not collected by cell
1265 sorting and put it between AG and T in UMAP plots.
1266
1267 **Figure S3 - Cell types in developing ferret cerebral cortex.**
1268 **A**. Dotplot showing average expression and percentage of expression of representative marker
1269 genes for individual cell types in the merged dataset. The largest cluster was composed of UL
1270 neurons, and their four clusters (Fig. 1**C**) were combined as a single "UL" group. P.E.,
1271 percentage of expressing cells per cell type; A.E., average expression per cell type.
1272 **B**. Percentage of sample collection stages in each cell type (top half) and percentage of each
1273 cell type in the merged dataset (bottom half).
1274 **C.** UMAP visualization of clusters split by their sample collection methods (AG or T) at each
1275 sampling stage.
1276 **D.** Heatmap showing the expression level of cell cycle marker genes based on log fold-change
1277 values. *PCNA*, *DUT*, *SIVA1,* and *TYMS* are markers of the S-phase; *UBE2C*, *CDCA4*, *CENPF,*
1278 and *CCNB1* are markers of the G2M-phase. Three subclusters among early RG, late RG, and
1279 IPC clusters expressed different markers for cell-cycle states. The color bar at the top indicates
1280 Seurat clusters matching those in Fig. 1**C**.
1281 **E.** Immunostaining for CRYAB$^+$ tRG (green) and HOPX$^+$ RG (red) together with DAPI on P1
1282 and P10 germinal layers.
1283
1284 **Figure S4 - Development of ferret tRG during postnatal cortical development.**
1285 **A.** Cellular features of a tRG cell in cortex labelled with GFP at embryonic stages via IUE.
1286 Vibratome sections at P0 and P4 (thickness = 200 μm) were immunostained for CRYAB
1287 (green) and GFP (red). CRYAB$^+$ truncated basal fibers spanned up to the SVZ.
1288 **B.** Pie charts showing the percentage of *CRYAB* expression in the ferret clusters of the merged
1289 transcriptome dataset of all stages (Fig. 1). Cells were counted as positive if unique molecular
1290 identifier counts for *CRYAB* were > 1 using Seurat "WhichCells" function (slot = "counts").
1291 **C.** Number of cells in the tRG clustered by age annotated in the ferret transcriptome dataset
1292 (Fig. 1).
1293 **D.** Number of *CRYAB*-expressing cells in RG clusters of the transcriptome dataset (Fig. 1).
1294 *CRYAB* expression was undetectable at E25. *CRYAB*-expressing cells in the midRG and lateRG

1295 subtypes did not change in all stages (cell numbers: 58, 46, 68, 55, and 61 at E34, E40, P1, P5,
1296 and P10, respectively), while the number of *CRYAB*$^{+}$ tRG cells increased after birth (cell
1297 numbers: 0, 21, 50, 91, and 118 at E34, E40, P1, P5, and P10, respectively).
1298 **E–G.** Violin plots indicating the normalized expression of *CRYAB* (**E**), *TBR2* or *EOMES* (**F**),
1299 and *OLIG2* (**G**) in the ferret clusters shown in Fig. 1.
1300
1301 **Figure S5 - Temporal fates of RG cells identified by pseudo-time trajectory analysis**
1302 **A.** Ferret cells used for pseudo-time trajectory analysis were lined up along the stretched
1303 pseudo-time axis. Expression levels of markers for typical cell types are also shown along the
1304 pseudo-time axis: *LIX1* and *HMGA2* for early RG, *EOMES* and *NEUROG2* for IP, *RGS20*, and
1305 *PTN* for late RG, *PDGFR* and *OLIG2* for glial cells, and *FOXJ1* and *FAM216B* for ependymal
1306 cells.
1307 **B.** Branching trees labelled by pseudo-time score. Color scale indicates log10 (pseudo-time
1308 +0.1) values. Each state is named after the major cell type.
1309 **C.** The composition of each state is shown by clusters defined in the UMAP plot (Fig. 1).
1310 Percentages for clusters were calculated from all cells in each state.
1311 **D.** Branching trees split by UMAP clusters (Fig. 1).
1312
1313 **Figure S6 - Ferret tRG adopt both ependymal and astrogenic fates in ferrets**
1314 **A.** Onset of ciliogenesis in the developing cortex of ferrets, shown via staining for ADENINE
1315 CYCLASE III (cyan) along the VZ surface at E40, P5, P10, and P35. Scale bars = 10 μm.
1316 **B.** Normalized expression of *SPARCL1*/cell in the major cell types shown in Fig. 1**C**.
1317 **C.** Plots showing *SPARCL1* mRNA count (left) and normalized FOXJ1 protein levels (right)
1318 in each cell clustered into individual classes (**A–D**) within the VZ shown in Fig. 4**H** (Table S4).
1319 The box and whisker plots indicate the range (lines) and the upper and lower quartiles with the
1320 median (box).
1321 **D.** Distances of each cell (its center of gravity) from the apical surface in the individual clusters
1322 (**A–D**), as indicated by the box and whisker plots in (**C**). Cluster C and D cells are significantly
1323 located on the apical surface compared to cluster B cells. Data normality was analyzed by
1324 Anderson-Darling test and statical significance was calculated by Kruskal-Wallis test with
1325 Dunn's multiple comparisons test.
1326
1327

1328 **Figure S7 - Comparison of molecular identity of RG subtypes between ferret and human**
1329 **A.** UMAP visualization of integrated ferret (n = 30,234) and human (n = 2,672) single-cell
1330 datasets colored according to the different clusters. The names of clusters from human and
1331 ferret cells begin with "H" and "F," respectively.
1332 **B.** Expression patterns of the indicated genes in each cluster. Circle color indicates the
1333 expression level of each gene. Circles size indicates the percentage of cells expressing the gene
1334 in the indicated cluster.
1335
1336 **Figure S8– The absence of a tRG cluster in human organoid datasets.**
1337 **A.** UMAP visualization of human organoid-driven cells colored by the original annotations for
1338 the cell line (left), age (middle) or state (right). Human organoid dataset from Bhaduri et al.,
1339 2020 was used. Bhaduri dataset contained organoids generated from 4 different lines, which
1340 showed a variability in terms of cell distribution on UMAP while overall temporal and
1341 differentiation axes were recapitulated.
1342 **B.** UMAP visualization of cells by clusters (left), original cluster annotations (middle), or by
1343 the normalized expression level of *CRYAB* (right). Red circles on UMAP highlight the group
1344 of cells expressing *CRYAB*. *CRYAB* expression was restricted to two out of four cell lines.
1345 CRYAB was expressed in clusters 26 and 30 enriched in the YH10 line, and cluster 29 enriched
1346 in the13234 cell line.
1347 **C-D.** UMAP visualization of integrated primary and organoid datasets from Bhaduri et al.,
1348 2020. Cells are colored by the originated dataset (left), primary tRG cluster (middle) or
1349 organoid dataset (right). Black circles were used to indicate the overlap of the region where
1350 human primary tRG was found. Human tRG did not overlap with organoid cells. We found
1351 that CRYAB-expressing organoid clusters 26 and 30 overlapped with "oRG/astrocyte" clusters
1352 of primary tissues.
1353 **E.** UMAP visualization of cells derived from Herring et al., 2022 human organoid dataset,
1354 colored by clusters (left) or by the normalized expression level of *CRYAB* (right).
1355
1356 **Figure S9 - Comparison of the tRG and oRG subtypes between ferrets and humans**
1357 **A, B** Matrices of correlations between two arbitrary RG subtypes from humans and ferrets by
1358 calculating marker gene scores as described for Fig. 5. (**A**) Correlations and (**B**) *p*-values
1359 between pairs in human and ferret clusters are shown. The early RG in ferrets showed the
1360 highest similarity with "OLIG1" in human data. This might be because of two reasons; (1) cells
1361 only at GW25 without early RG were used for comparison, and (2) cells in "OLIG1" highly

expressed genes related with cell proliferation, as the early RG also did (Table S6). We did not observe any cell types in human data corresponding to the ferret "midRG" with the same reason described above.

C Distribution of human and ferret tRGs in the integrated dataset. The number in the X-axis indicates the cluster number identified by the UMAP in Fig. 6C.

D Expression pattern of the subtype maker genes in the three tRG-enriched clusters (7, 21, and 28).

E Expression patterns of *CRYM*, *CLU*, and *HOPX* in oRG cells and other NPCs in humans.

F *In situ* hybridization of *CLU* at the ferret cortex showed its expression in all VZ, ISVZ, and OSVZ at P5.

Figure.1. Cell types in developing ferret cerebral cortex.

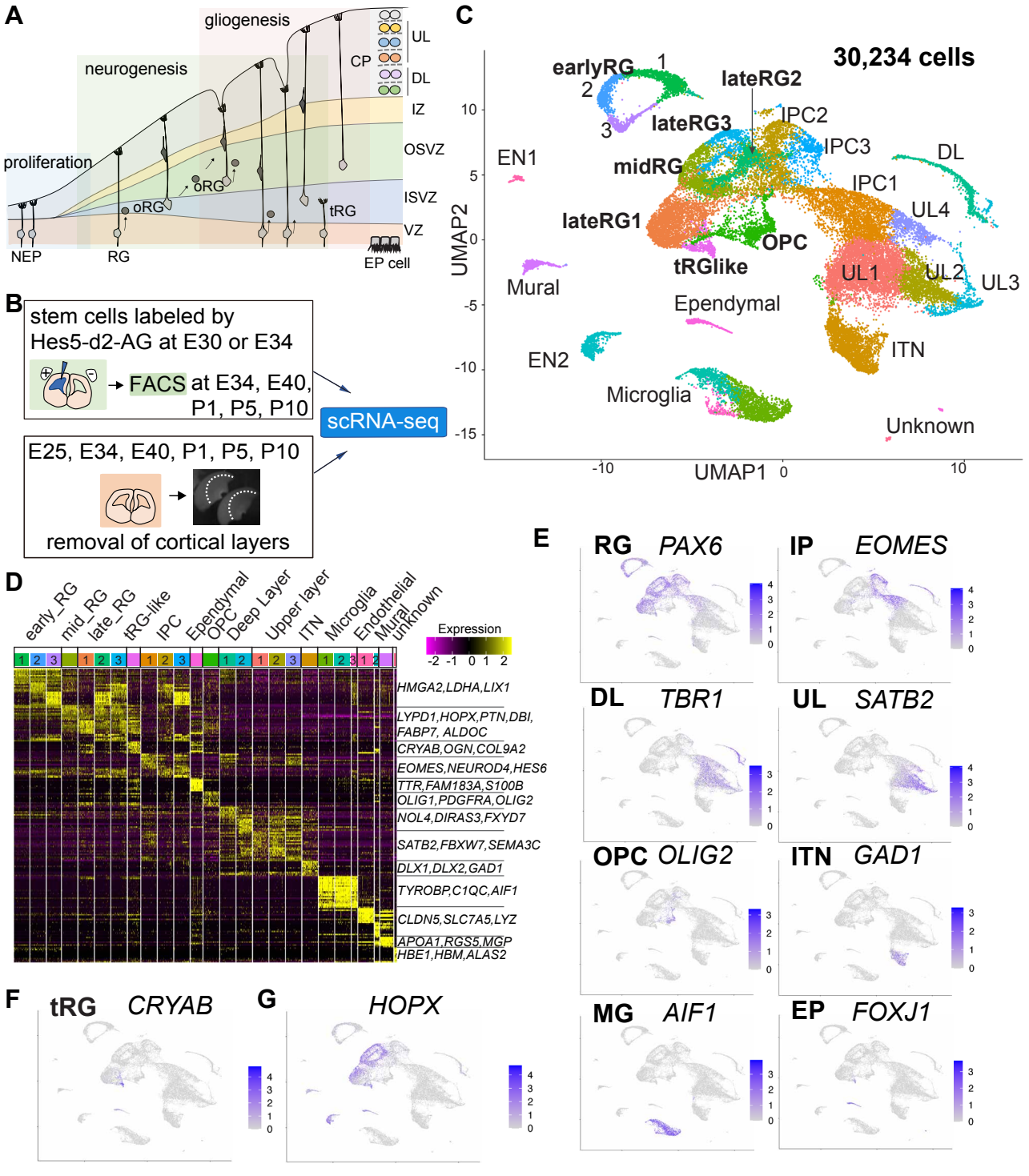

Figure 2. Emergence of ferret tRG during post-natal cortical development.

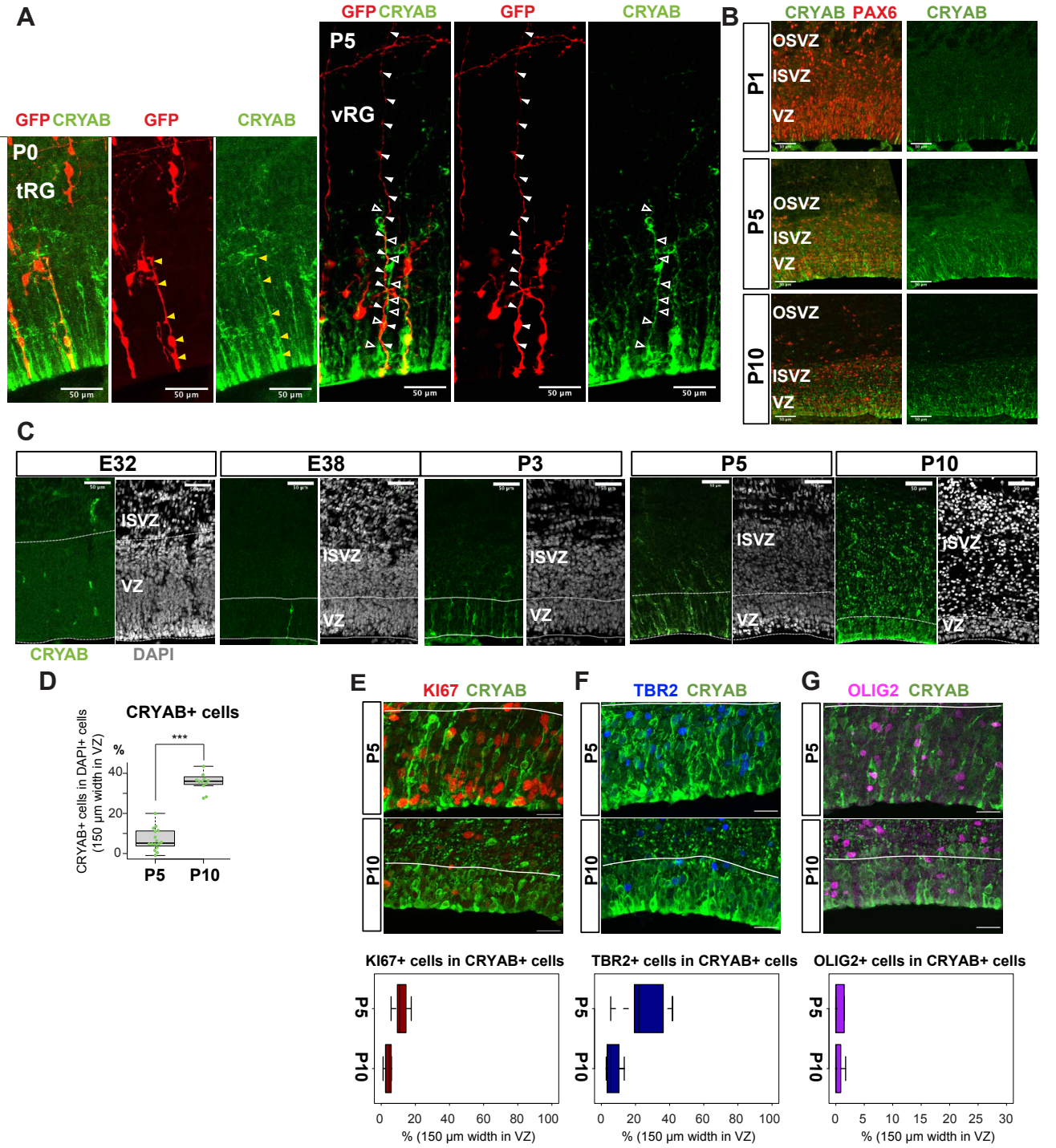

Figure 3. Temporal fates of RG cells predicted by pseudo-time trajectory analysis.

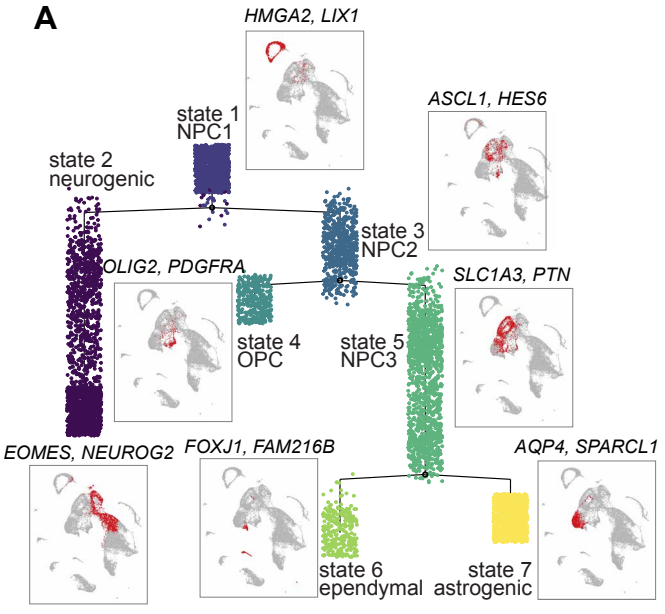

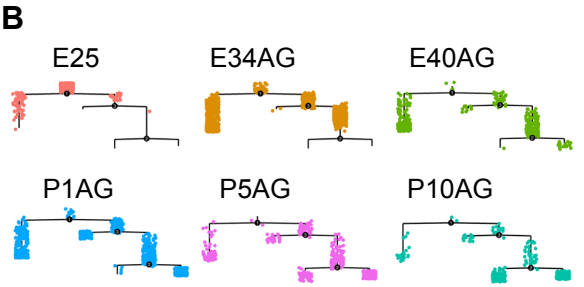

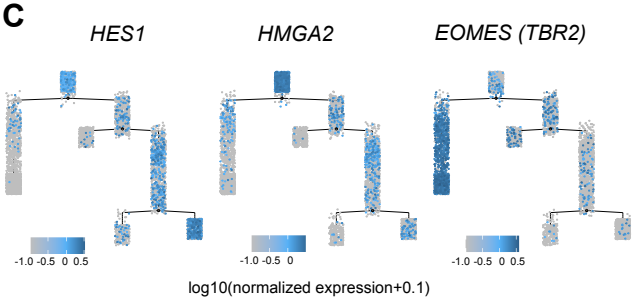

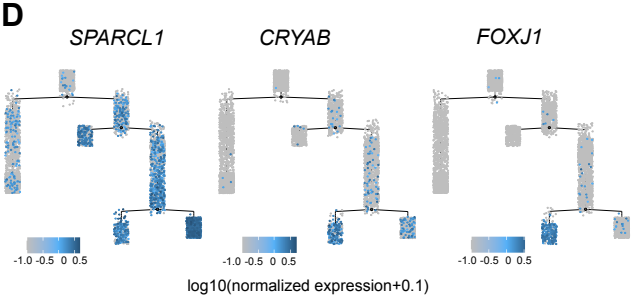

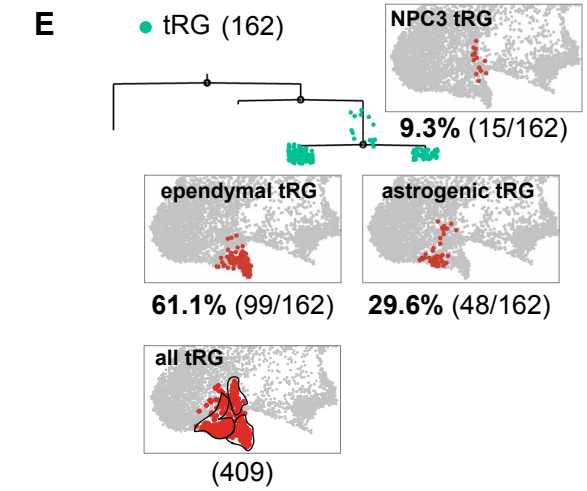

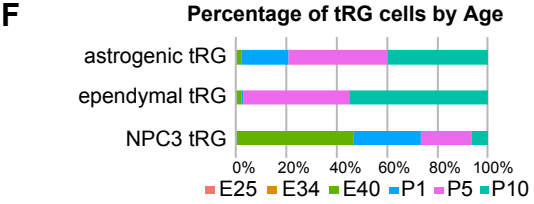

Figure 4. tRG adopt both ependymal and astrogenic fates in ferrets.

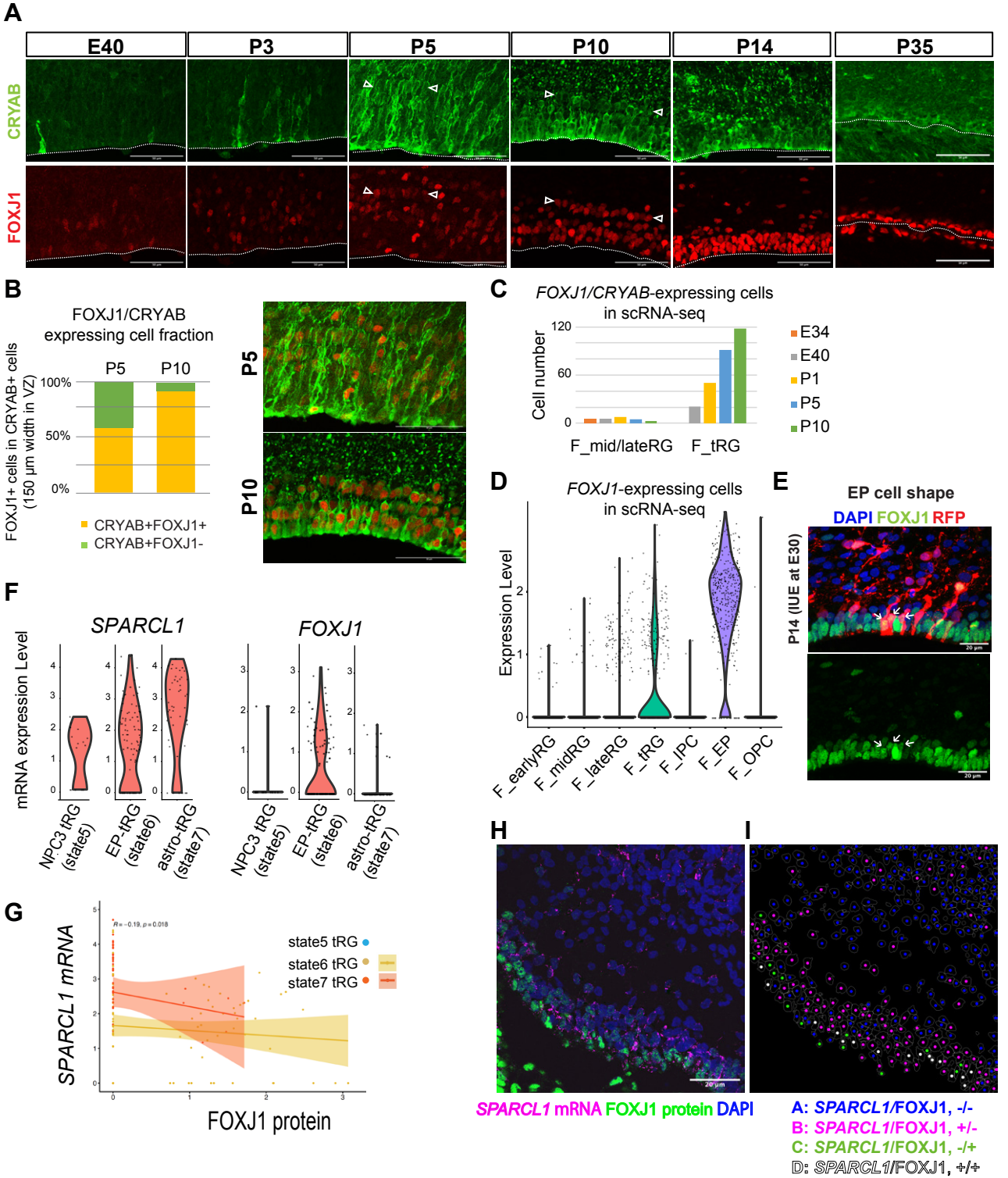

Figure 5. Comparison of molecular identity of RG subtypes between ferret and

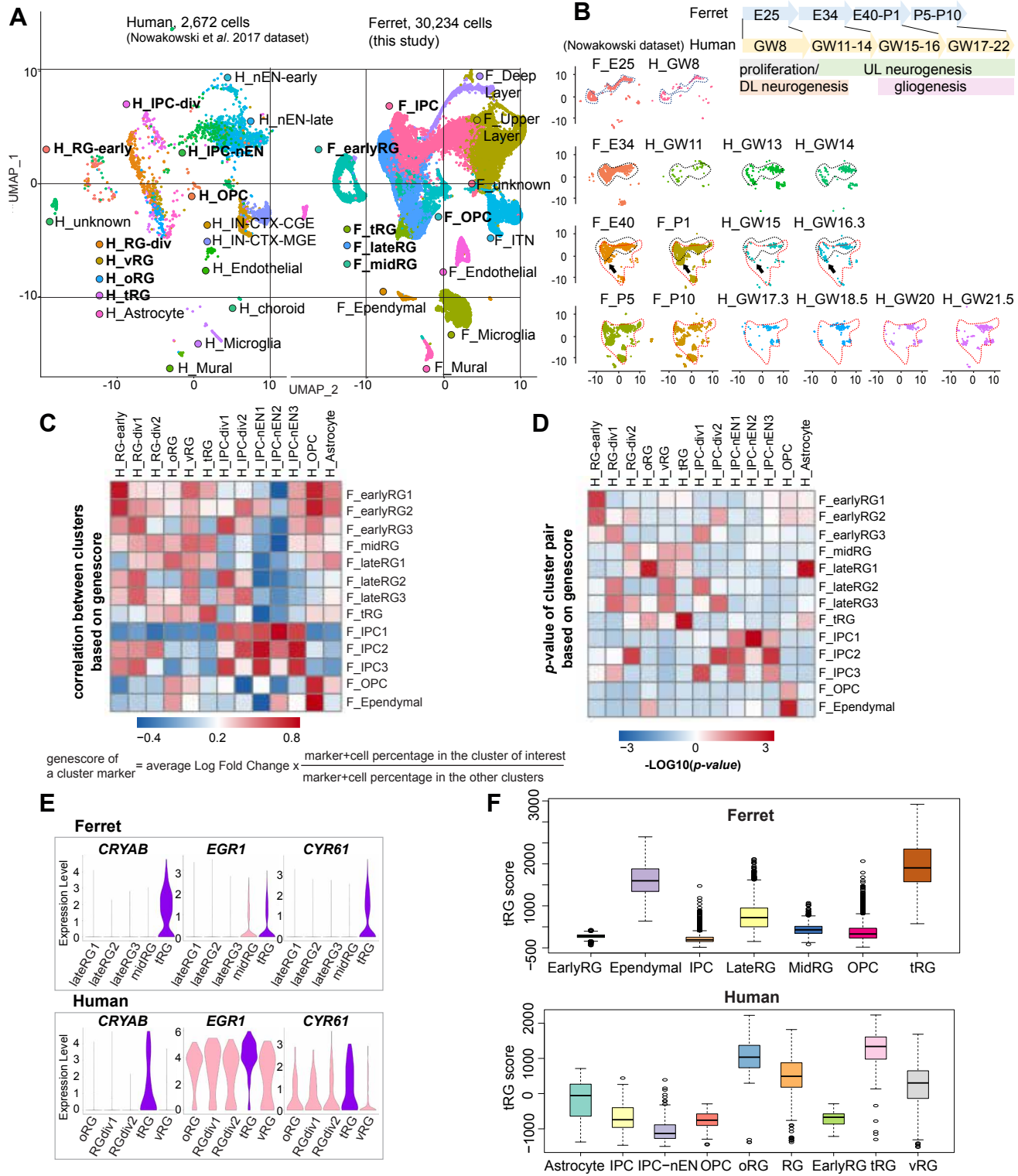

Figure 6. Comparison of the tRG and oRG subtypes between ferrets and humans.

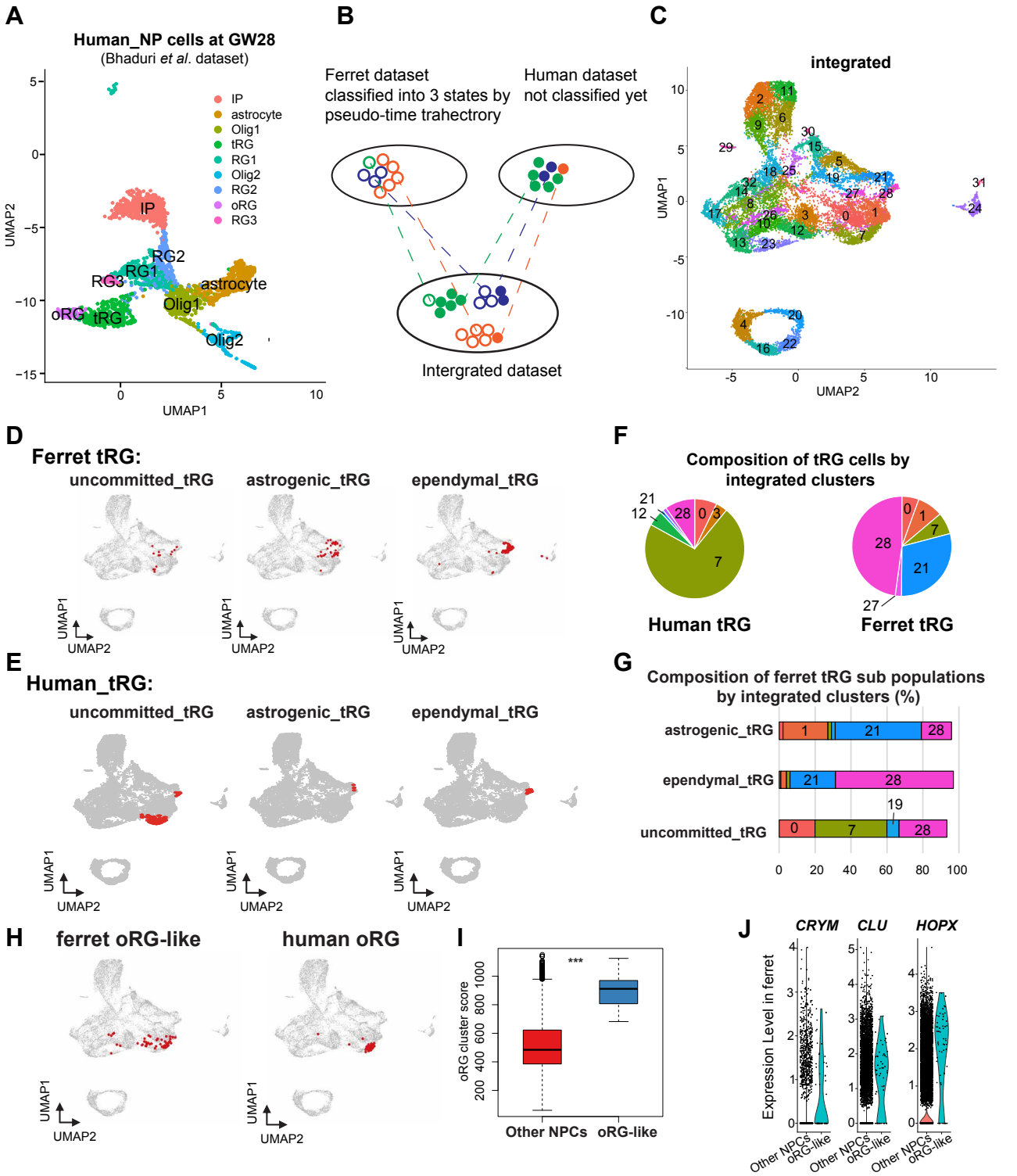

Figure S1. Development of the ferret cerebral cortex.

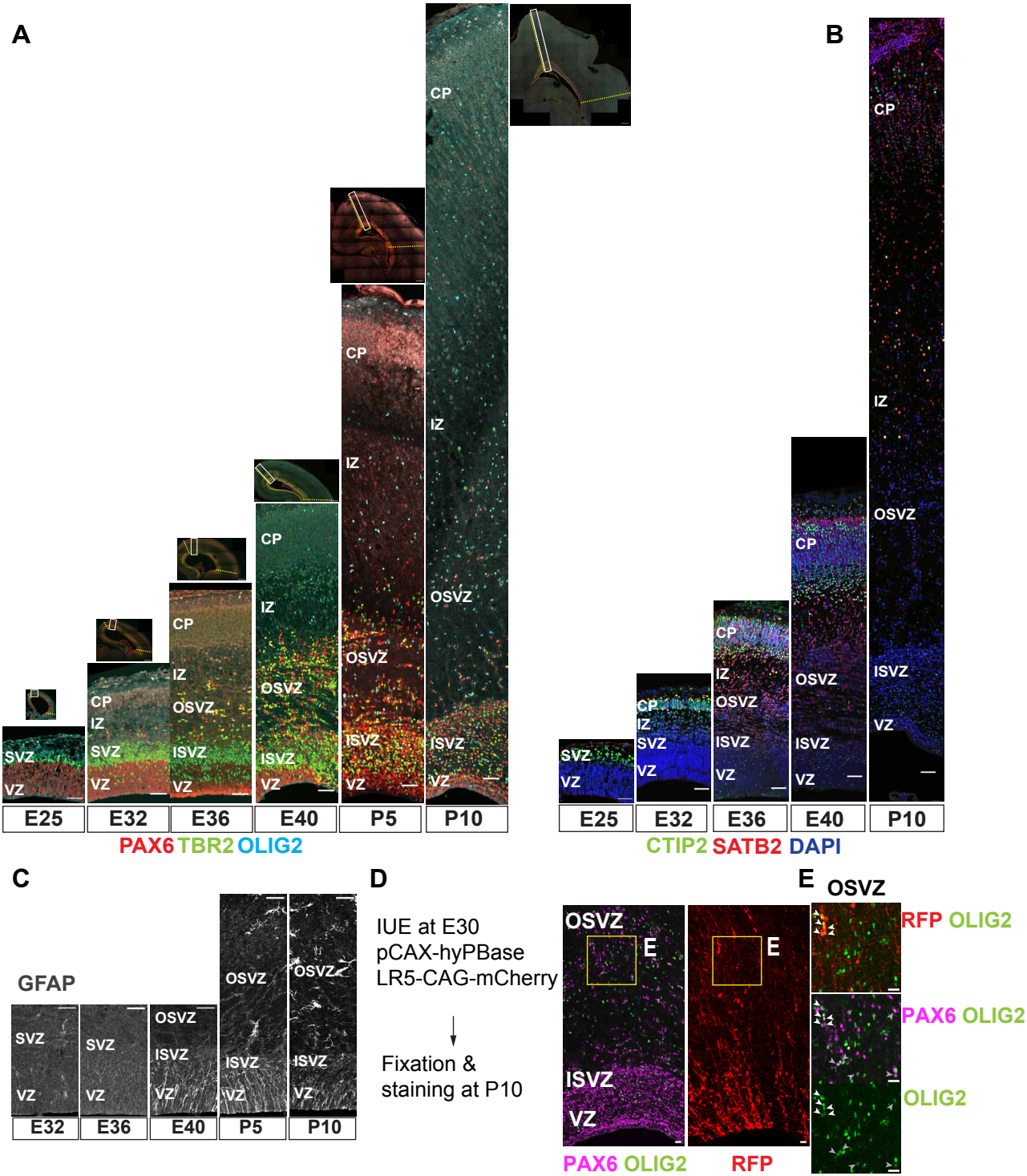

Figure S2. Cell types in developing ferret cerebral cortex.

A

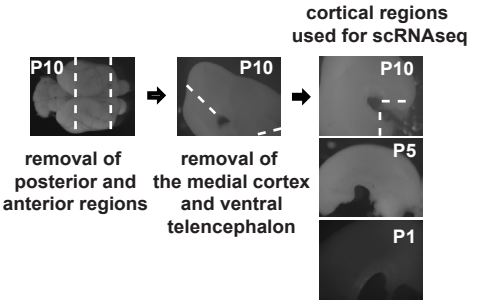

B

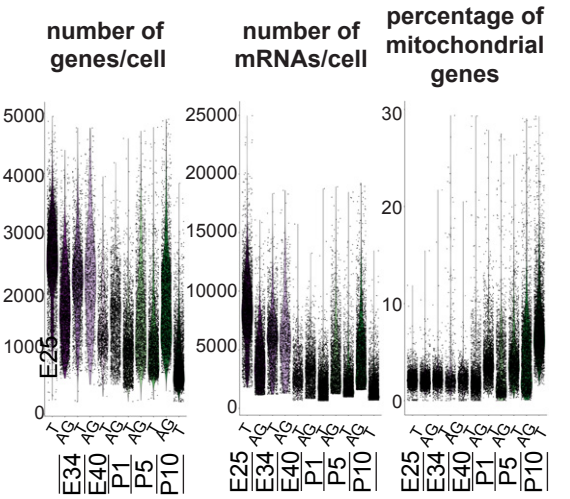

C

	Reference	Estimated Number of Cell	Median Genes per Cell	Number of Reads	Reads Mapped to Transcriptome	Total Genes Detected	Median UMI Counts
E34_AG	NCBI	3,226	953	137,673,935	30.70%	14,562	2,153
E34_AG	This study	3,223	1,763	137,673,935	58.20%	17,886	3,983
E34_T	NCBI	2,260	1,182	107,508,876	29.90%	14,445	3,096
E34_T	This study	2,265	2,195	107,508,876	56.40%	17,838	5,863

D

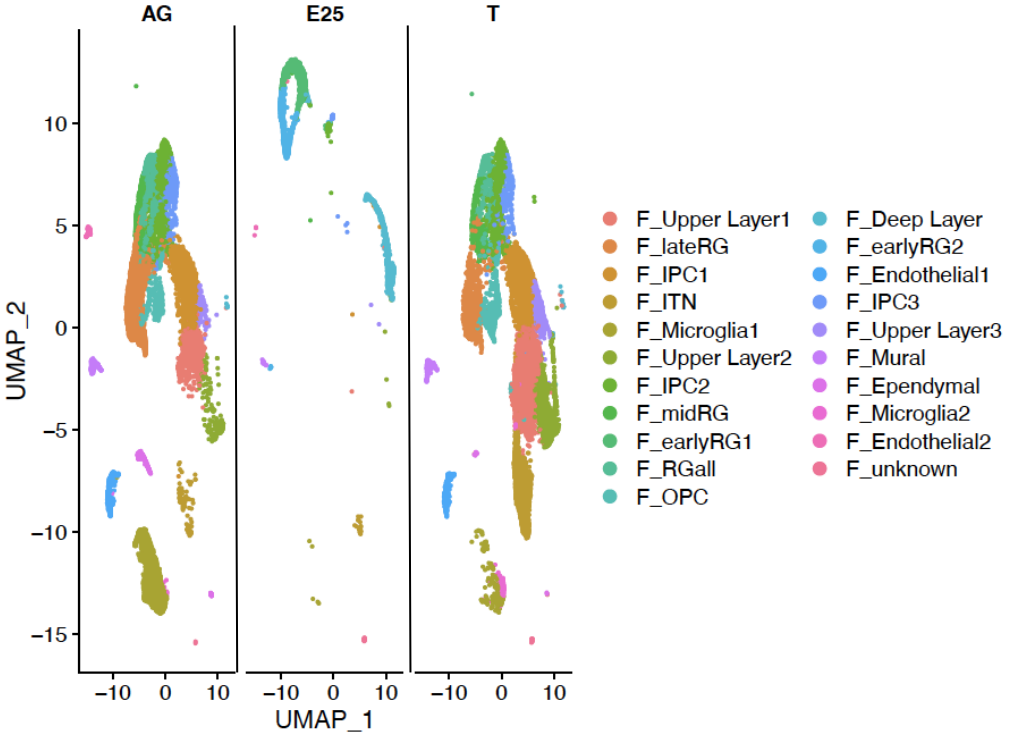

Figure S3. Cell types in developing ferret cerebral cortex.

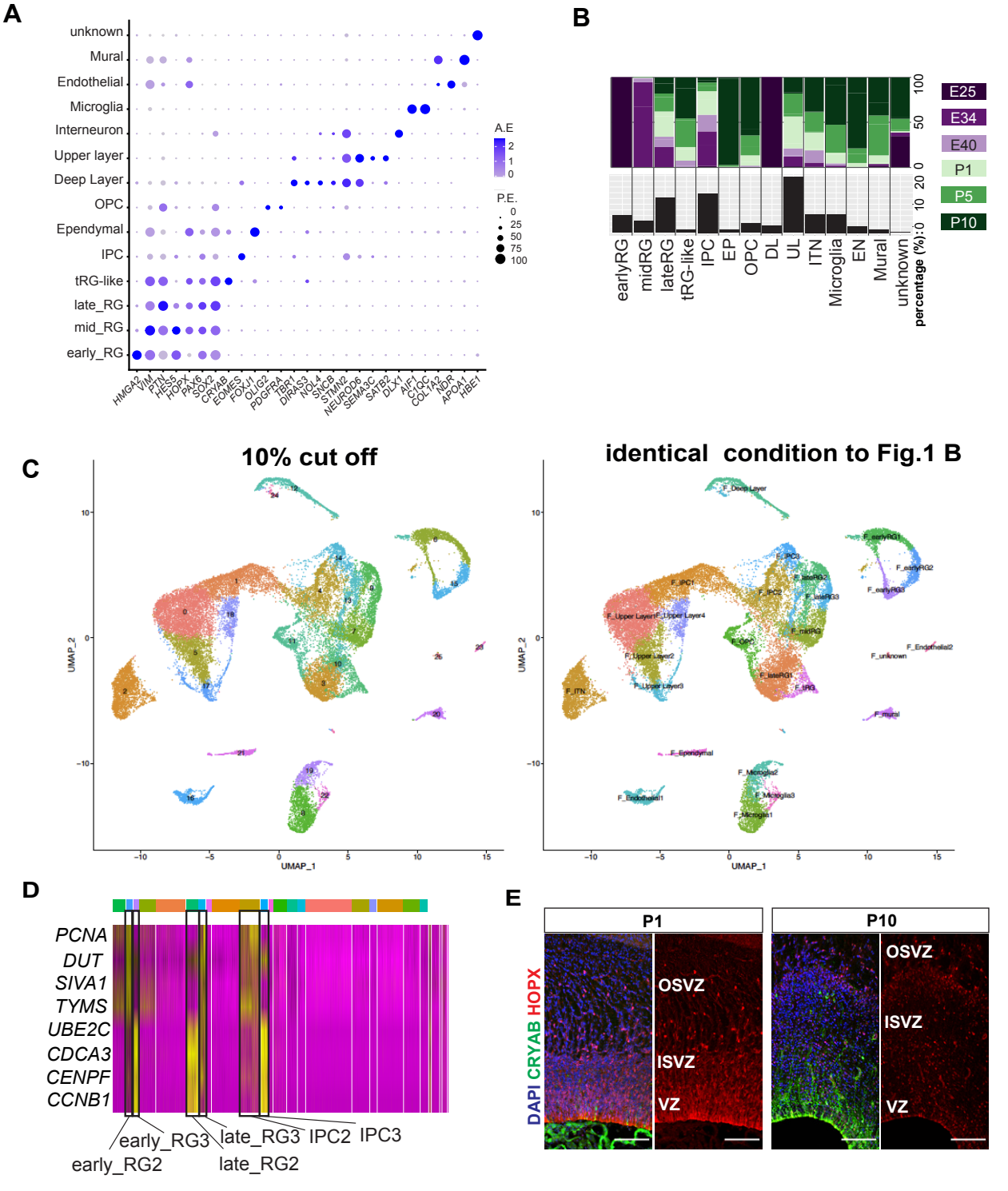

Figure S4. Development of ferret tRG during post-natal cortical development.

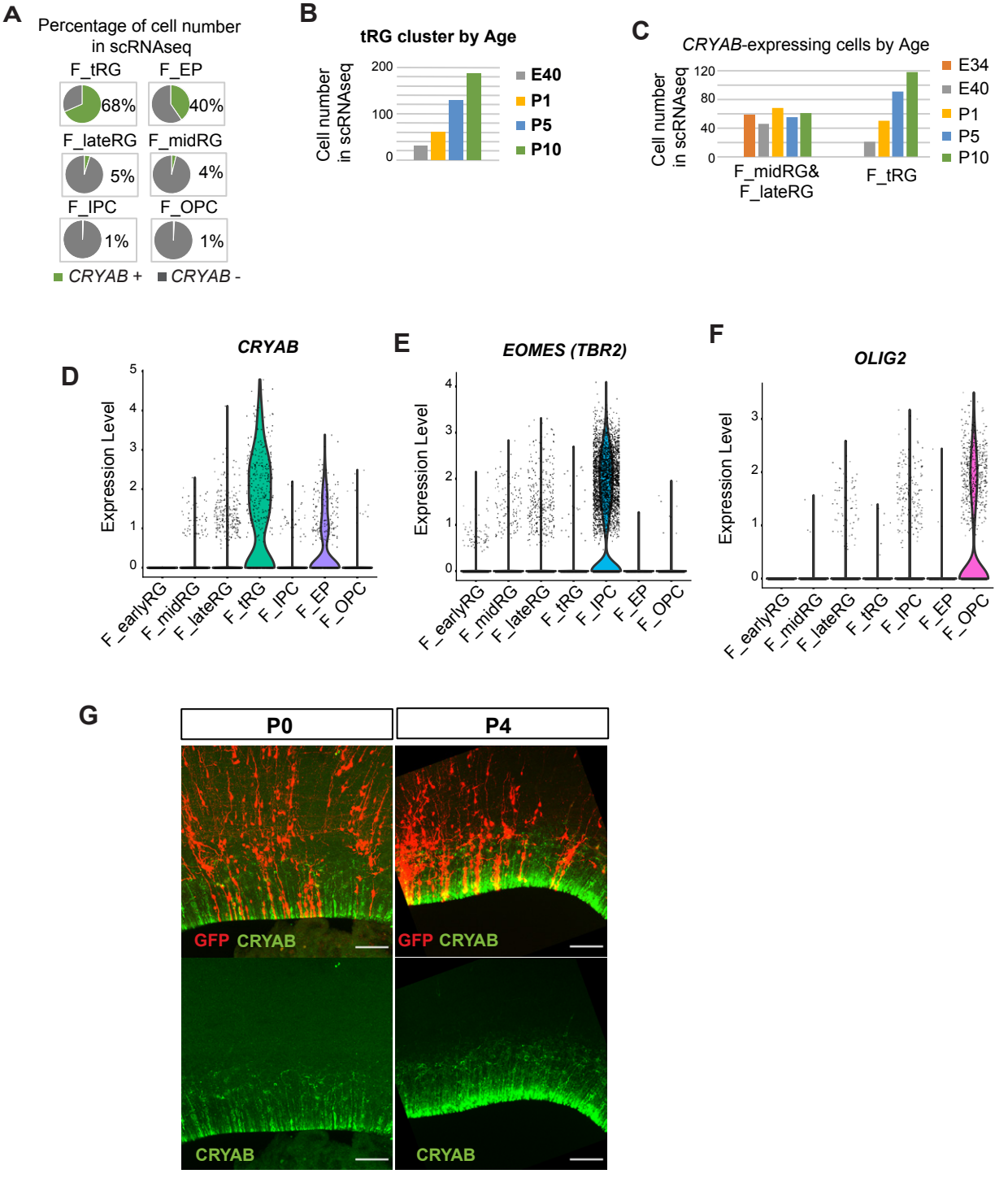

Figure S5. Temporal fates of RG cells predicted by pseudo-time trajectory analysis.

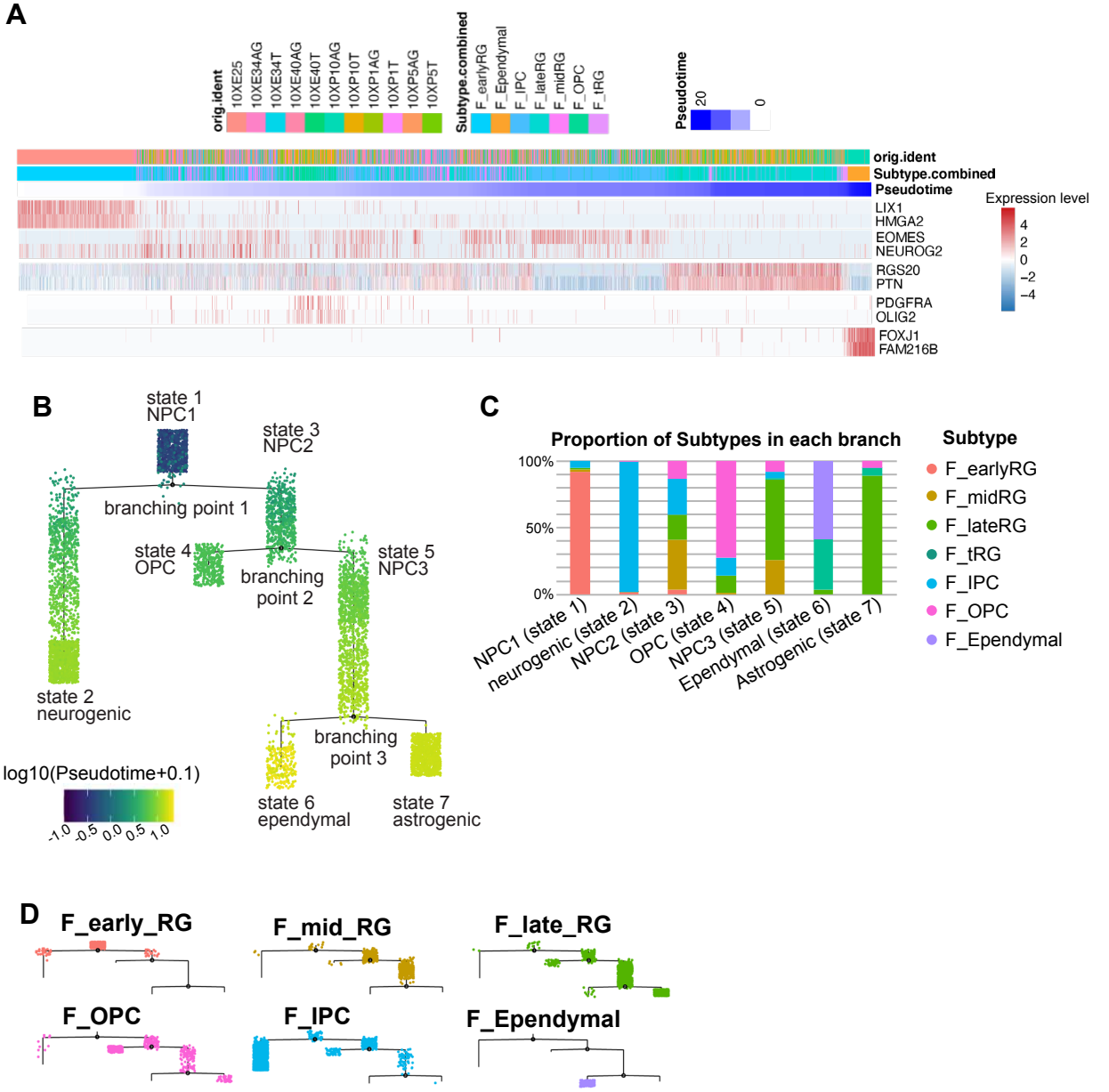

Figure S6. tRG adopt both ependymal and astrogenic fates in ferrets.

A

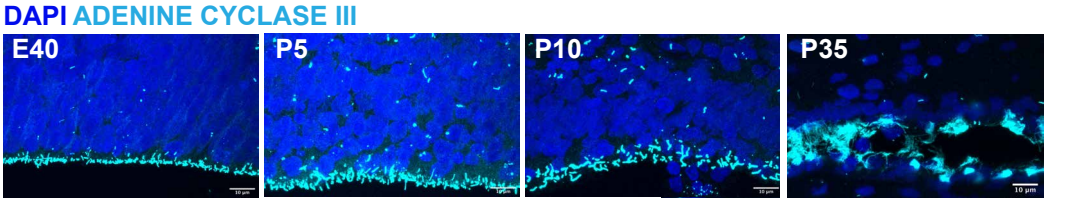

B

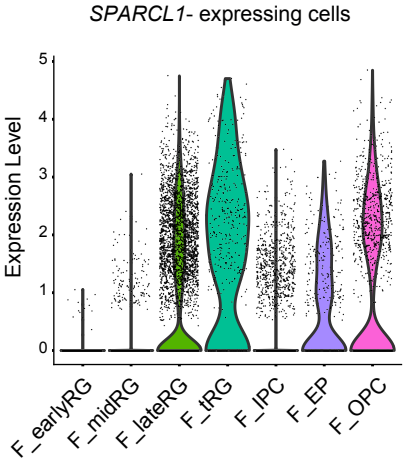

C

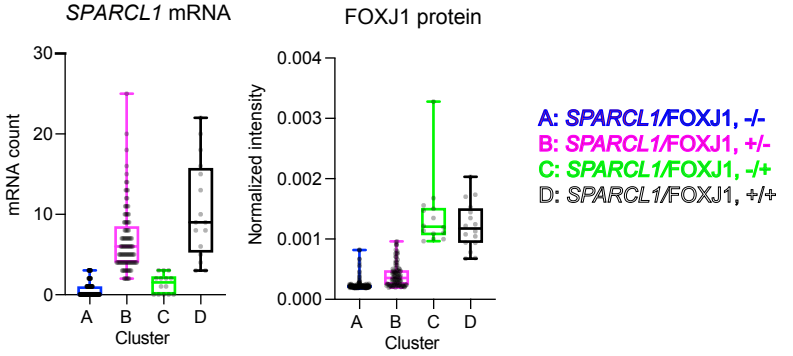

D

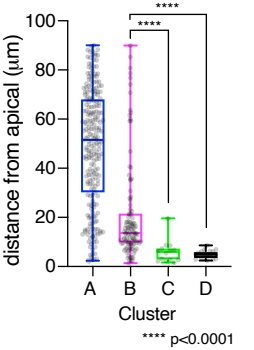

Figure S7. Comparison of molecular identity of RG subtypes between ferret and human.

A

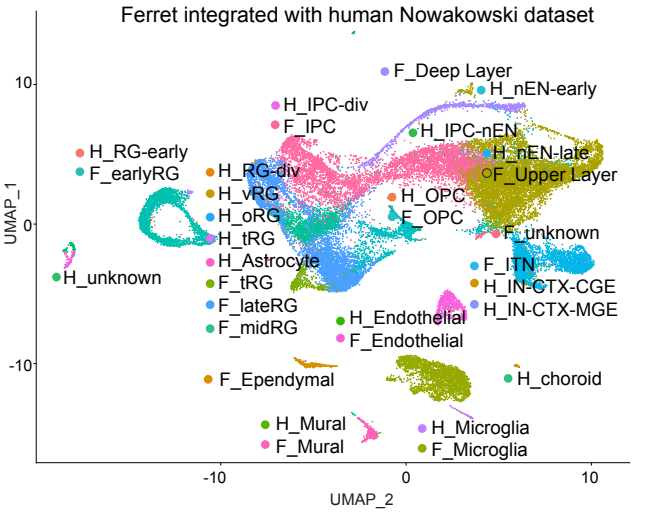

B

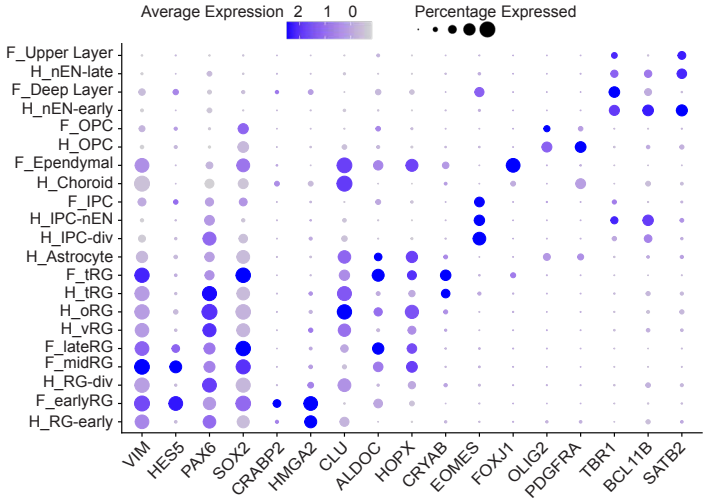

Figure S8. single cell analysis of cortical organoid dataset (Bhaduri et al., 2020)

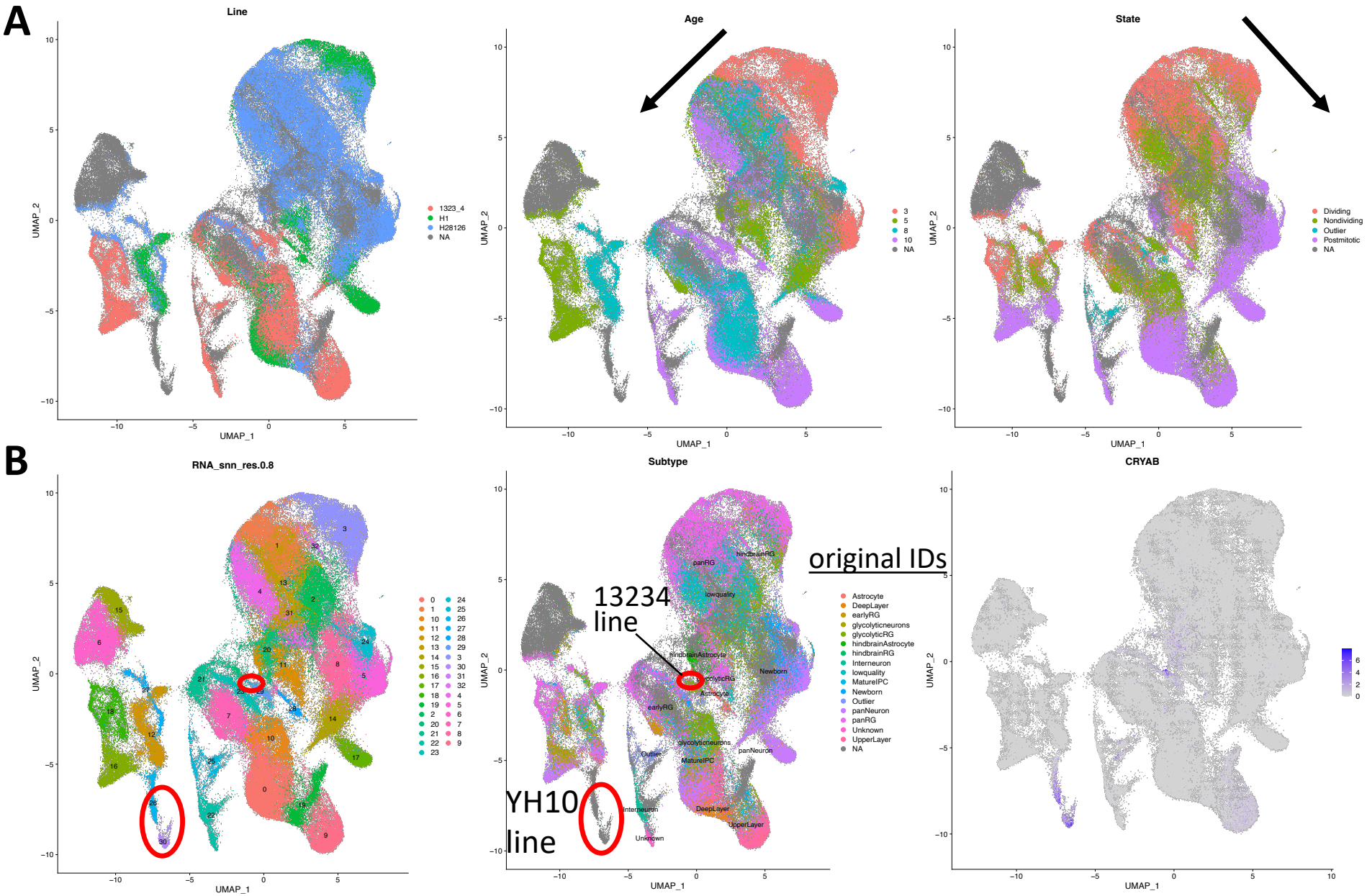

C

Integrated organoid and primary datasets (Bhaduri et al., 2020)

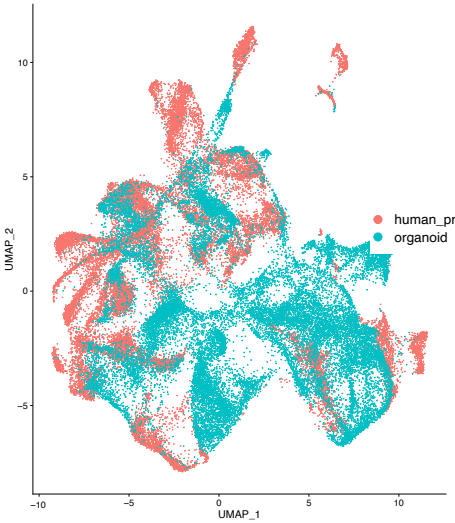

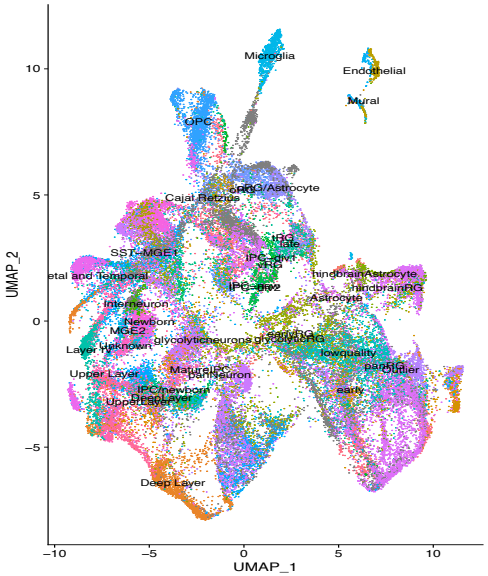

original IDs of primary dataset

- Astrocyte
- Cajal Retzius
- Deep Layer
- DeepLayer
- early
- earlyRG
- Endothelial
- glycolyticneurons
- glycolyticRG
- hindbrainAstrocyte
- hindbrainRG
- Interneuron
- IPC−div1
- IPC−div2
- IPC−new
- IPC/newborn
- late
- Layer IV
- lowquality
- MatureIPC
- MGE2
- Microglia
- Mural
- Newborn
- OPC
- oRG
- oRG/Astrocyte
- Outlier
- panNeuron
- panRG
- Parietal and Temporal
- SST−MGE1
- tRG
- Unknown
- Upper Layer
- UpperLayer
- vRG
- NA

D

primary tissue tRG (red)

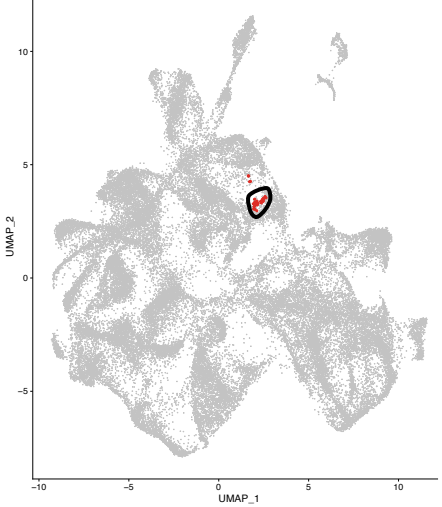

all organoid cells (red)

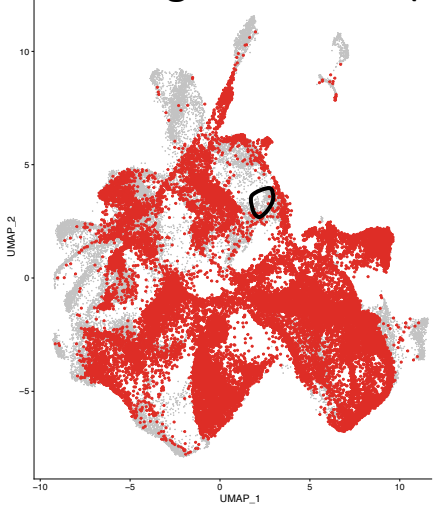

integrated clusters

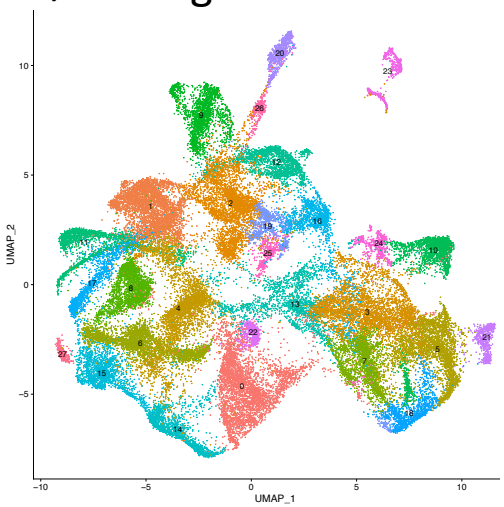

organoid clusters

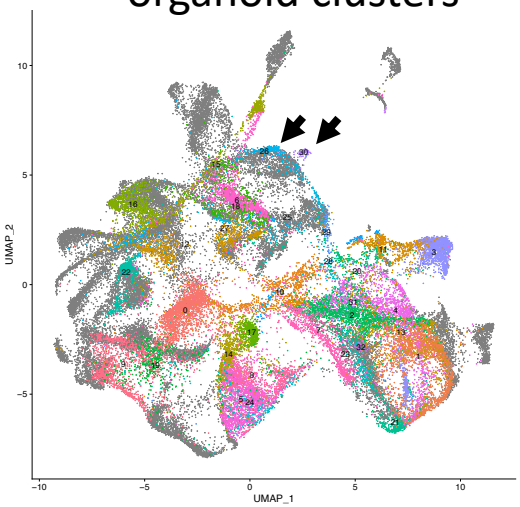

Herring et al., 2022 organoid dataset

E

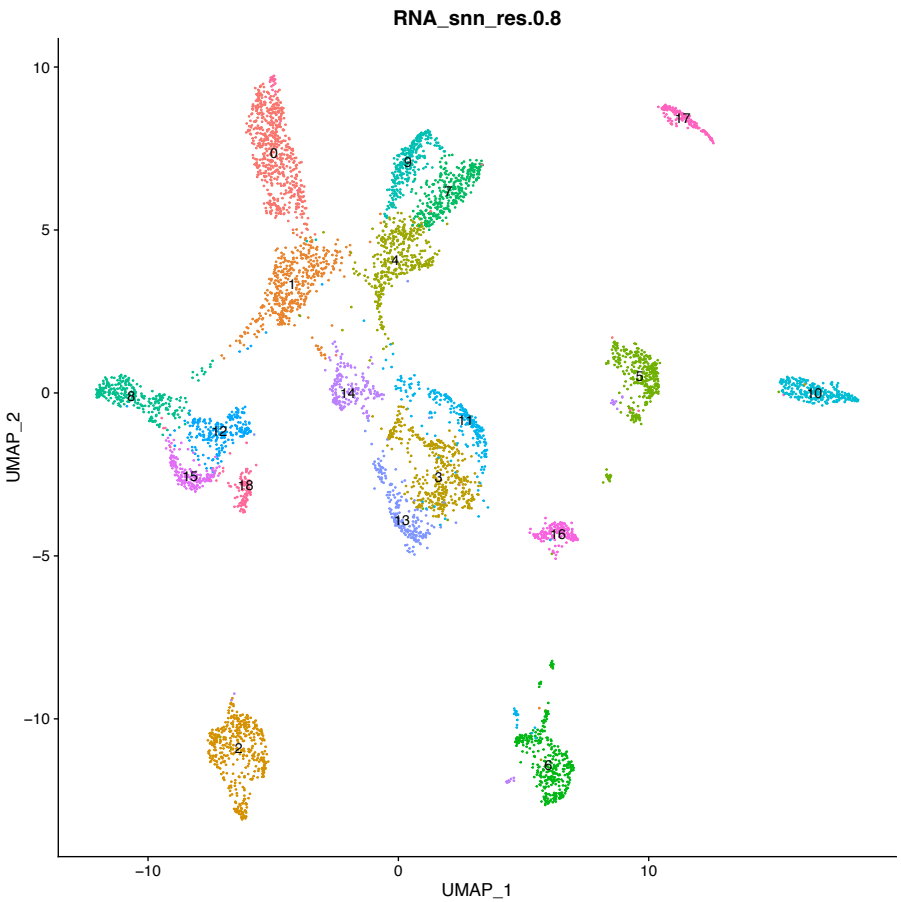

F

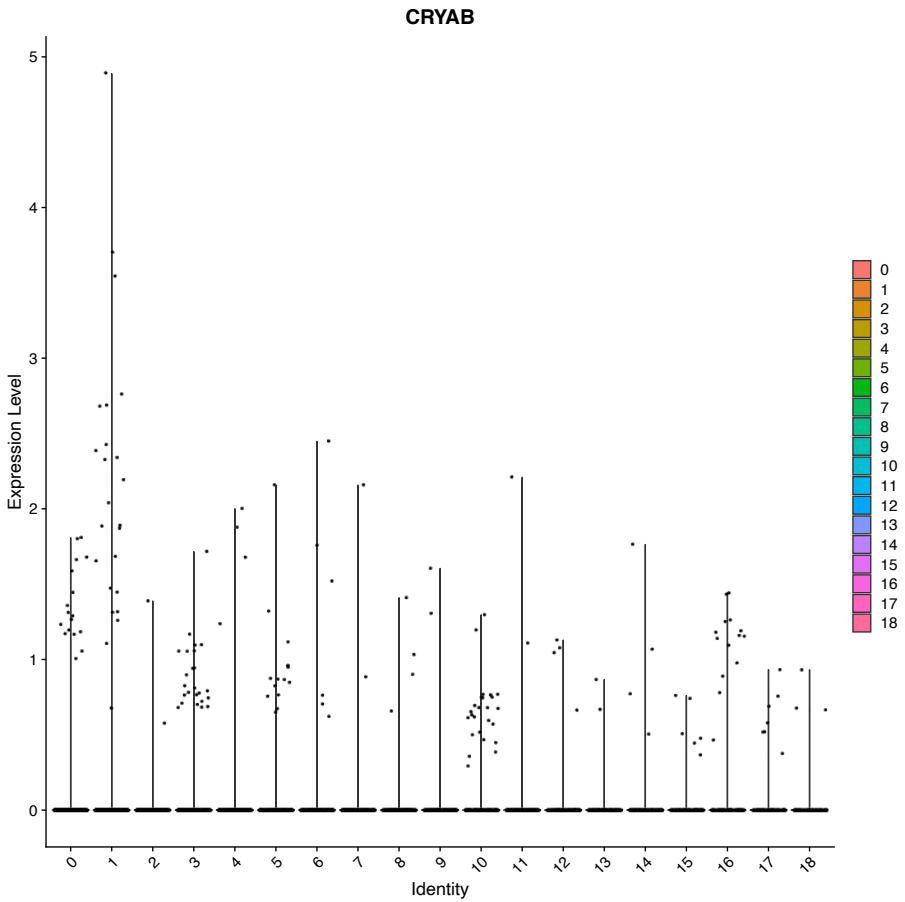
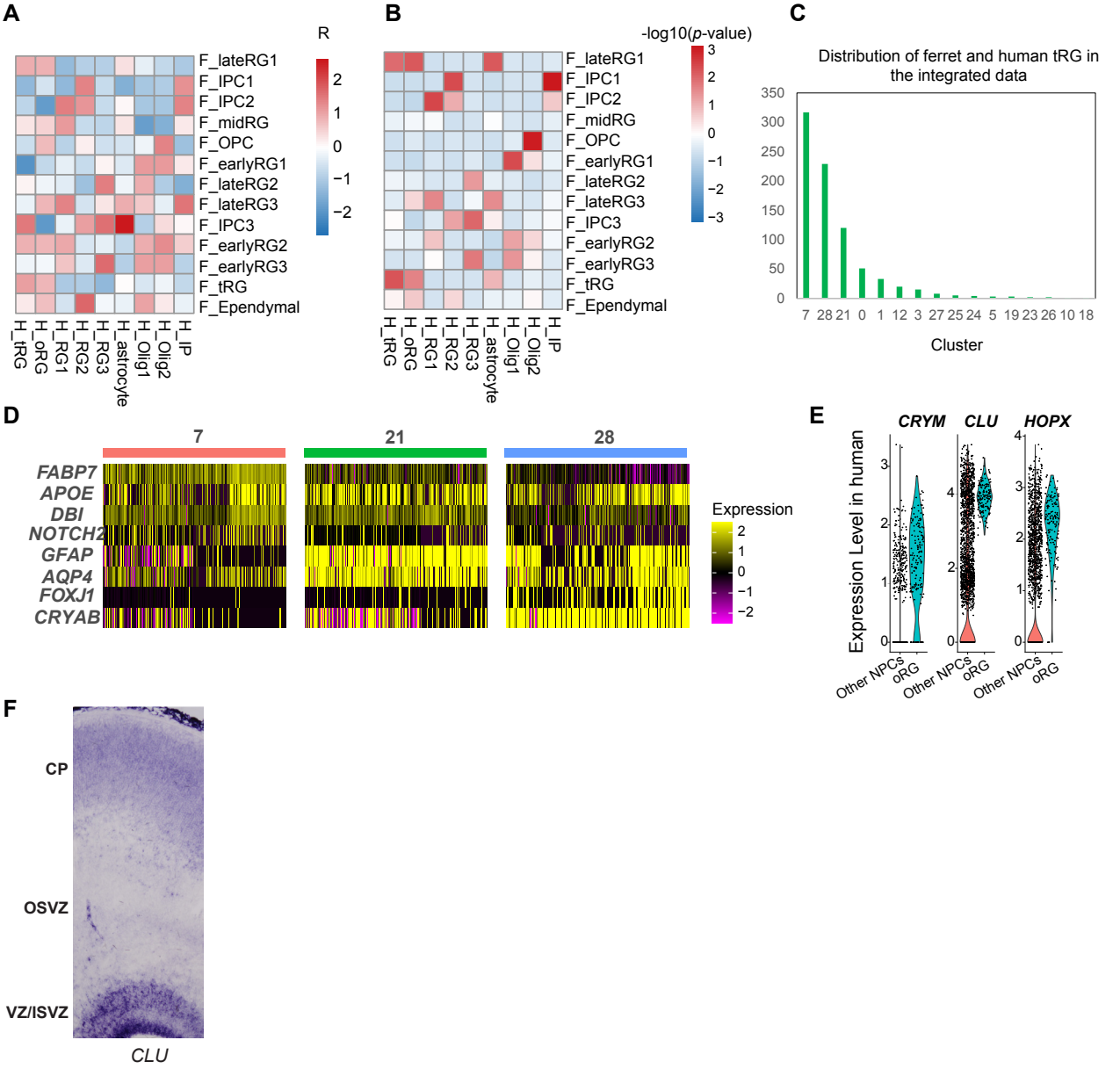
Figure S9. Comparison of the tRG and oRG subtypes between ferrets and humans.